SPECIAL
DYNAMO/CINDY/AMIE/LASP
COLLECTION

Diurnal Cycle of Precipitation Features Observed during DYNAMO

MARQUETTE N. ROCQUE[a] AND STEVEN A. RUTLEDGE[a]

[a] *Department of Atmospheric Science, Colorado State University, Fort Collins, Colorado*

(Manuscript received 16 July 2020, in final form 26 April 2021)

ABSTRACT: This study uses shipborne (R/V *Roger Revelle* and R/V *Mirai*) radar, upper-air, ocean, and surface meteorology datasets from the DYNAMO field campaign to investigate the diurnal cycle (DC) of precipitation over the central Indian Ocean related to two distinct Madden–Julian oscillations (MJOs) observed. This study extends earlier studies on the MJO DC by examining the relationship between the DC of convective organization and the local environment and comparing these results on- and off-equator. During the suppressed phase on-equator, the DC of rain rates exhibited two weak maxima at 1500 and 0100 LT, which was largely controlled by the presence of sub-MCS nonlinear precipitation features (PFs). During the active phase on-equator, MCS nonlinear features dominated the rain volume, and the greatest increase in rain rates occurred between 2100 and 0100 LT. This maximum coincided with the maxima in convective available potential energy (CAPE) and sensible heat flux, and the column moistened significantly overnight. Off-equator, the environment was much drier and there was little large-scale upward motion as a result of limited deep convection. The DC of rain rates during the active phase off-equator was most similar to the DC observed during the suppressed phase on-equator, while rainfall off-equator during the suppressed phase did not vary much throughout the day. The DC of MCS nonlinear PFs closely resembled the DC of rainfall during both phases off-equator, and the DC of environmental parameters, including sea surface temperature, CAPE, and latent heat flux, was typically much weaker off-equator compared to on-equator.

KEYWORDS: Madden-Julian oscillation; Air-sea interaction; Mesoscale processes; In situ atmospheric observations; Radars/Radar observations

1. Introduction

Despite numerous studies, the Madden–Julian oscillation (MJO; Madden and Julian 1971, 1972), a large-scale tropical phenomenon which contributes the majority of intraseasonal variability and bridges the realm between weather and climate (Zhang 2005, 2013), is still not well simulated by numerical models and therefore has low predictability (Bechtold et al. 2008; Kim et al. 2009; Vitart and Molteni 2010; Lin et al. 2006; Hung et al. 2013). Cloud and precipitation parameterizations are considered to be the primary cause of poor model performance for the MJO (Randall et al. 2003; Lin et al. 2006; Zhang et al. 2006; Benedict and Randall 2009; Zhao and Nasuno 2020). To improve these parameterizations, it is important to fully understand the connection between convective organization (squall type versus nonsquall type, mesoscale versus submesoscale in terms of feature size, etc.) and the environment in the context of the MJO. Another particular interest is the diurnal cycle (DC) of precipitation over the Indian Ocean (IO), where the MJO forms, from both modeling and observational perspectives. The lack of in situ observations in the IO to investigate each of these processes was a primary motivator for the Dynamics of the MJO (DYNAMO) field campaign in late 2011–early 2012 (Yoneyama et al. 2013). The resulting dataset from DYNAMO is extensive and includes radar, radiosonde, ocean, and surface data from ships and islands in the central IO. In the current study, this dataset will be used to improve our understanding of how the convective organization of precipitation features (PFs) impacts the precipitation DC and how convective organization varies between the suppressed and active phases of the MJO. Additionally, this study directly contrasts the convective populations and associated DCs on- and off-equator (0° and 8°S).

The evolution of convective organization and its relationship to the environment needs to be well understood to accurately simulate the DC of rainfall. Convective organization plays a major role in the general circulation and energy budget through horizontal and vertical heat and momentum fluxes and has been shown to impact the hydrological cycle (Rickenbach and Rutledge 1998, hereafter RR98; Cheng et al. 2018, and references therein). RR98 analyzed the radar population from the Tropical Ocean and Global Atmosphere Coupled Ocean–Atmosphere Response Experiment (TOGA COARE) and found that MCSs (linear and nonlinear) had the highest rain rates, while sub-MCS nonlinear events were present most often. Xu and Rutledge (2015, hereafter XR15) performed a similar analysis with the DYNAMO radar population and determined MCS events represented only 10% of the population but contributed 70% of the total precipitation, with sub-MCS nonlinear features occurring most frequently. XR15 analyzed the population by MJO phase and found sub-MCS

Corresponding author: Marquette N. Rocque, marquette.rocque@colostate.edu

DOI: 10.1175/JAS-D-20-0215.1

features were dominant in the suppressed phase and MCSs were far more prevalent in the active phase. Several studies have also connected convective organization to the local environment by analyzing the air–sea fluxes, sea surface temperature (SST), and lower tropospheric moisture (Saxen and Rutledge 1998; XR15; Skyllingstad et al. 2019). Studies have shown air–sea fluxes are highest in the active phase (Saxen and Rutledge 1998; Yokoi and Yoneyama 2014; XR15; Sakaeda et al. 2018) and are coupled to MCS events (Saxen and Rutledge 1998). For example, descending rear inflows (Smull and Houze, 1985), which can increase near-surface winds, act to enhance sensible and latent heat fluxes. The recent modeling study by Skyllingstad et al. (2019) showed that air–sea fluxes were key factors in convective forcing, with latent heat flux becoming increasingly important in higher background wind simulations ($U = 12\,\mathrm{m\,s^{-1}}$). These higher wind simulations also produced smaller, disorganized cells, while weaker wind simulations ($U = 6\,\mathrm{m\,s^{-1}}$) produced persistent linear systems. Results from a modeling study by Zhao and Nasuno (2020) suggest that models need to have high-frequency air–sea coupling (less than 1-h temporal scale) to accurately depict SSTs and convection during the MJO. Thus, the complex interaction between convective organization and the environment can have a large impact on the amount of precipitation, especially when these parameters vary throughout the day.

Numerous studies have been conducted that examined the DC of convection over land and ocean using satellite observations, rain gauge measurements, and radar-based estimates. Results from these studies have consistently revealed a maximum in oceanic convection during the early morning hours (0000–0600 LT; Gray and Jacobson 1977; Janowiak et al. 1994; Chen and Houze 1997; Sui et al. 1997; Yang and Slingo 2001; Tian et al. 2006; Suzuki 2009; Sakaeda et al. 2017, 2018; Rowe et al. 2019). Several mechanisms have been proposed to explain this nighttime maximum including differential radiative cooling (Gray and Jacobson 1977), increases in tropospheric moisture (Sui et al. 1997; Ruppert and Johnson 2015), and the life cycle of convective systems (Chen and Houze 1997). This nighttime maximum is found in both active and suppressed phases of the MJO. Studies have also shown the suppressed phases of the MJO exhibit an additional peak in rainfall during the afternoon hours (Chen and Houze 1997; Sui et al. 1997; Tian et al. 2006; Suzuki 2009; Ruppert and Johnson 2015; Sakaeda et al. 2017, 2018). This afternoon maximum has been hypothesized to be related to heating of the ocean's surface and the creation of diurnal warm layers in the near-surface layer (Bellenger et al. 2010; Moum et al. 2014; Thompson et al. 2018). During the active phase, ocean surface heating is not as pronounced, and diurnal warm layers are not typically present because of the enhanced cloudiness from larger disturbances and associated higher wind speeds. Thus, the afternoon peak in rainfall is not observed (Bellenger et al. 2010). Additionally, several studies have reported differences in rainfall and the DC of rainfall between different locations within the tropics, including the IO and west Pacific (Tian et al. 2006; Suzuki 2009; Xu et al. 2015; Sakaeda et al. 2017). In particular, Xu et al. (2015) used radar data from DYNAMO to investigate rainfall statistics at three sites within the IO, two on-equator sites (Gan Island and R/V *Roger Revelle*) and one off-equator site (R/V *Mirai*). They found a strong MJO signal on-equator, but the off-equator site was only weakly impacted by the MJO, with more shallow warm rain convection and considerably less mesoscale organization. The on-equator sites were about 800 km apart and also exhibited differences, with more gradual deepening of convection at the eastern site, and more variability in precipitation at the western site. Quantifying these local differences is important for understanding the MJOs influence both within and beyond the convective envelope.

Until DYNAMO, most of the studies that examined the DC of oceanic convection used satellite data due to the lack of in situ measurements in the central IO. Specifically, early studies used infrared brightness temperatures to categorize convection by cloud-top height (Janowiak et al. 1994; Chen and Houze 1997; Sui et al. 1997; Yang and Slingo 2001; Tian et al. 2006; Suzuki 2009), but this method currently has difficulty distinguishing precipitating from nonprecipitating clouds and convective from stratiform clouds. More recent studies have used the Tropical Rainfall Measuring Mission (TRMM) precipitation algorithm to analyze the DC of convection (Nesbitt et al. 2000; Liu et al. 2008; Liu and Zipser 2013), but resolution limitations prevent isolated convection from being fully resolved (Kummerow et al. 1998; Huffman et al. 2007). This study sets out to examine the DC of MJO precipitation and determine the contributions of PF type to the DC using high-resolution radar data. To further our understanding of the MJOs impact within the central IO, results from the R/V *Roger Revelle* on-equator and R/V *Mirai* off-equator are directly contrasted.

2. Data and methodology

This study uses DYNAMO sounding, surface meteorological, oceanographic, and radar data from the R/V *Roger Revelle* (hereafter *Revelle*) and the R/V *Mirai* (hereafter *Mirai*). For this study, the primary focus was on the strongest and most complete MJO cycles during DYNAMO which occurred in October and November 2011 (Yoneyama et al. 2013; Gottschalck et al. 2013; Xu and Rutledge 2014; XR15). To ensure the results represented an open ocean environment at a consistent location, data were only analyzed when the ships were on station.

a. Sounding and ship-based data

The DYNAMO sounding array consisted of six sites in the domain, two of which were on the *Revelle* and *Mirai* (Johnson and Ciesielski 2013, hereafter JC13). Most days have sounding data available every three hours (JC13). The sounding dataset includes directly measured and derived parameters interpolated to a 5-hPa vertical grid (JC13) and quality controlled with details found in Ciesielski et al. (2014).

Both the *Revelle* and *Mirai* were outfitted with a suite of instruments to measure surface and atmospheric parameters (Moum et al. 2014; Yokoi and Yoneyama 2014; de Szoeke et al. 2015). The ship-based surface data were recorded in 10-min intervals throughout DYNAMO. Most meteorological instruments were located on the forward mast of both ships, whereas SST was measured by a towed thermistor known as a sea snake. The sea snake was set to a depth of 5 cm for the duration of the cruises, and a warm layer correction was applied following the field campaign (Edson et al. 2017).

The latent and sensible heat fluxes from both ships were calculated using the COARE 3.5 bulk flux algorithm (Edson et al. 2013; de Szoeke et al. 2015). The COARE algorithm uses a combination of ocean and atmospheric parameters to compute bulk air–sea fluxes based on the equations $Q_s = \rho c_p C_h |u| \Delta T$ and $Q_L = \rho L_v C_e |u| \Delta q$, where Q_s is sensible heat flux, Q_L is latent heat flux, ρ is surface air density, c_p is the specific heat of air at constant pressure, L_v is the latent heat of vaporization, C_h and C_e are transfer coefficients, $|u|$ is 10 m wind speed, and ΔT and Δq are temperature and specific humidity differences between the ocean and the near-surface atmosphere ($\mathrm{SST} - T_{\mathrm{air}}$; $\mathrm{SSq} - q_{\mathrm{air}}$; Fairall et al. 1996, 2003; Edson et al. 2013; de Szoeke et al. 2015).

b. ERA5

ERA5 data (Copernicus Climate Change Service 2017) were used to examine the large-scale flow and surface conditions over the central IO. The reanalysis dataset has $0.25^\circ \times 0.25^\circ$ resolution (approximately 28 km horizontal grid spacing in the DYNAMO array), 37 vertical grid levels, and hourly temporal resolution. Any latitudinal or longitudinal averaging applied was calculated ±5 grid points from the *Revelle* or *Mirai* locations to represent the approximate radar domains.

c. Radar data

Both the *Revelle* and *Mirai* operated C-band radars for the duration of their respective cruises. The National Aeronautics and Space Administration (NASA) TOGA radar on board the *Revelle* was operated by Colorado State University (CSU) and NASA and cycled through designed radar scans every 10 min (Xu et al. 2015), collecting radar reflectivity, Doppler velocity, and spectral width. The radar on board the *Mirai* was operated by the Japan Agency for Marine-Earth Science and Technology (JAMSTEC) and also cycled through scans every 10 min (Xu et al. 2015). The *Revelle* radar data were quality controlled by CSU and NASA (details in Xu and Rutledge 2014), and an attenuation correction algorithm, derived from the drop size distribution collected during DYNAMO (Thompson et al. 2015), was applied to reflectivity. Similar quality control and attenuation corrections were applied to the *Mirai* radar by JAMSTEC (Katsumata et al. 2008) and CSU (Xu et al. 2015). After a preliminary analysis of the *Mirai* data, it was found that sea clutter was still abundant. Additional filtering was performed on the *Mirai* radar which masked all pixels with an echo-top height less than 2 km.

d. Radar-derived products

After quality control was performed, the polar-coordinate radar data were interpolated to a grid with horizontal and vertical resolutions of 1 and 0.5 km, respectively (Dolan et al. 2017). From the gridded data, radar reflectivity was classified as either convective or stratiform using the algorithm detailed in Steiner et al. (1995). We note that this algorithm does have limitations, especially in the tropical oceans where isolated and weak convection, with reflectivity values less than 40 dBZ, is frequently categorized as stratiform (Powell et al. 2016). Thus, we classified all grid points associated with isolated PFs as convective in nature. From this classification, convective and stratiform rain rates were calculated using Z–R relationships derived from the DYNAMO drop size distribution measurements (Thompson et al. 2015). Convective rain rate is given by $Z = 130.51R^{1.45}$ and stratiform rain rate is derived from $Z = 294.61R^{1.55}$ (Xu and Rutledge 2014). These relationships were applied to both the *Revelle* and *Mirai* radars.

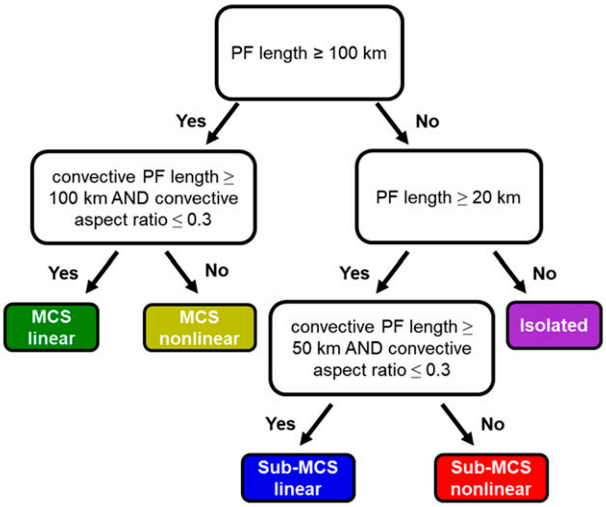

FIG. 1. PF identification framework.

e. Radar-based PFs

To study PF organization and intensity as a function of MJO phase and DC, a PF identification algorithm, similar to ones used in TRMM PF studies (Nesbitt et al. 2000, 2006; Liu et al. 2008; Liu and Zipser 2013; XR15), was employed that automatically classified each PF in a given radar volume. This identification algorithm fits an ellipse to each PF and calculates the major and minor axes of the ellipse (Medioni et al. 2000; Nesbitt et al. 2006; XR15). From each ellipse, statistics including the length, area, convective/stratiform partitioning, convective/stratiform rain rates, and radar echo statistics can be derived. This study included PFs with at least 0 dBZ reflectivity values at 2 km above mean sea level (MSL), unlike past TRMM Precipitation Radar studies which could only detect PFs greater than 17 dBZ. This algorithm also produces statistics from convective-only ellipses, which were calculated around at least 20 contiguous pixels defined as convective [using the Steiner et al. (1995) algorithm] within a given PF. The convective ellipse was used to classify systems as linear versus nonlinear, based on the configuration of the convective elements internal to the PF.

Once PFs were identified, they were classified into one of five categories. These categories were based on a PF morphology study conducted by RR98 using radar data from TOGA COARE. The flow diagram for PF classification is shown in Fig. 1. The length of the total PF ellipse determines whether the feature is MCS, sub-MCS, or isolated (i.e., isolated features are <20 km in length, sub-MCS scales range from 20 to 100 km, and MCS features are >100 km in length). The length and aspect ratio (defined as the ratio of the minor to major axis) of the associated convective ellipse then determines whether the PFs

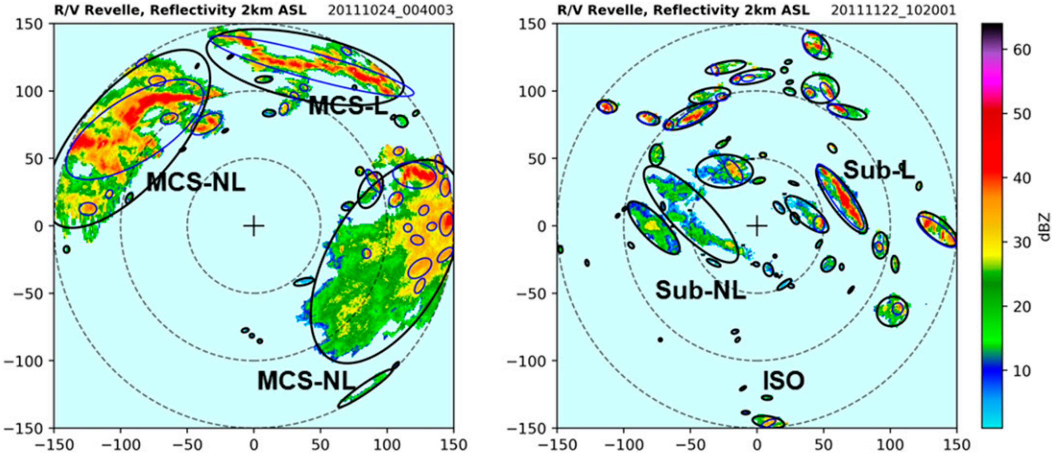

FIG. 2. Examples of different PF morphologies from the *Revelle*. MCS-L (MCS linear), MCS-NL (MCS nonlinear), SubL (sub-MCS linear), SubNL (sub-MCS nonlinear), and ISO (isolated). Black ellipses represent total PFs while blue ellipses represent convective PFs.

are linear or nonlinear (i.e., linear events have a convective aspect ratio < 0.3). This method differs from XR15 who used the aspect ratio of the overall PF ellipse to determine linearity, but we assume that the linearity is better defined by the convective elements of the PF, not the overall PF area. Radar examples of each PF type are shown in Fig. 2.

f. MJO indices

To determine which days represented the suppressed or active MJO phase, the Wheeler–Hendon Real-Time Multivariate MJO (RMM) index (Wheeler and Hendon 2004) was used. The RMM index was computed using the large-scale outgoing longwave radiation and 850 and 200 hPa zonal wind and has been shown to be an effective representation of MJO activity in the tropics (Lau and Wu 2010; Riley et al. 2011; Barnes and Houze 2013). MJO phases correspond to an RMM index between one and eight. At the *Revelle*, phases 1–3 were associated with an active MJO, and phases 5–8 were generally associated with suppressed MJO conditions (Xu and Rutledge 2014; Ciesielski et al. 2018). Between October and November, 25 days were classified as suppressed and 30 days were classified as active. However, this study only analyzed data when the ships were on station, so there were 15 days representing the suppressed phase (5–15 October; 12–17 November) and 27 days representing the active phase (15–28 October; 17 November–1 December) at the *Revelle*, and 25 days in both phase groups (active: 15–24 October; 1–4 November; 17–29 November; suppressed: 1–15 October; 6–17 November) at the *Mirai*. The associated number of PFs identified within each phase at each location is shown in Table 1.

g. Statistical testing

A binomial signs test was used to determine if differences between active and suppressed phase environmental parameters were statistically significant at the 95% confidence level. This test is beneficial since it does not require any assumptions about the underlying distributions of the data. Furthermore, this test works equally well with small and large sample sizes.

3. MJO evolution

The focus of this study is on two MJOs that occurred during DYNAMO in October (MJO1) and November (MJO2) 2011 (Xu and Rutledge 2014). In addition to the MJOs, there were also embedded equatorial Rossby waves and Kelvin waves that passed over the DYNAMO array and contributed to the precipitation accumulation (Gottschalck et al. 2013). These synoptic-scale waves have been shown to contribute to the DC of rainfall (Rowe et al. 2019). However, we will not specifically investigate the role of synoptic waves in this study.

During the suppressed phase in the beginning of October, the large-scale circulation over the *Revelle* was weak (Fig. 3a). There was weak subsidence throughout the column and little convergence near the surface. Off-equator the intertropical convergence zone (ITCZ) was active, and there was a maximum in upward motion achieved near 6°S. The extent of the ITCZ reached from about 2°–9.5°S, with the *Mirai* capturing a fair amount of mesoscale activity. At the surface within the

TABLE 1. Distribution of the number of PFs within each category (isolated, sub-MCS nonlinear, sub-MCS linear, MCS nonlinear, MCS linear) and phase at the *Revelle* and *Mirai*.

Phase	Suppressed	Active
Revelle	(15 days)	(27 days)
Isolated	84 960	182 640
Sub-MCS nonlinear	6884	23 469
Sub-MCS linear	23	125
MCS nonlinear	183	2811
MCS linear	1	62
Mirai	(25 days)	(25 days)
Isolated	312 392	187 593
Sub-MCS nonlinear	18 510	10 553
Sub-MCS linear	23	35
MCS nonlinear	1403	709
MCS linear	35	30

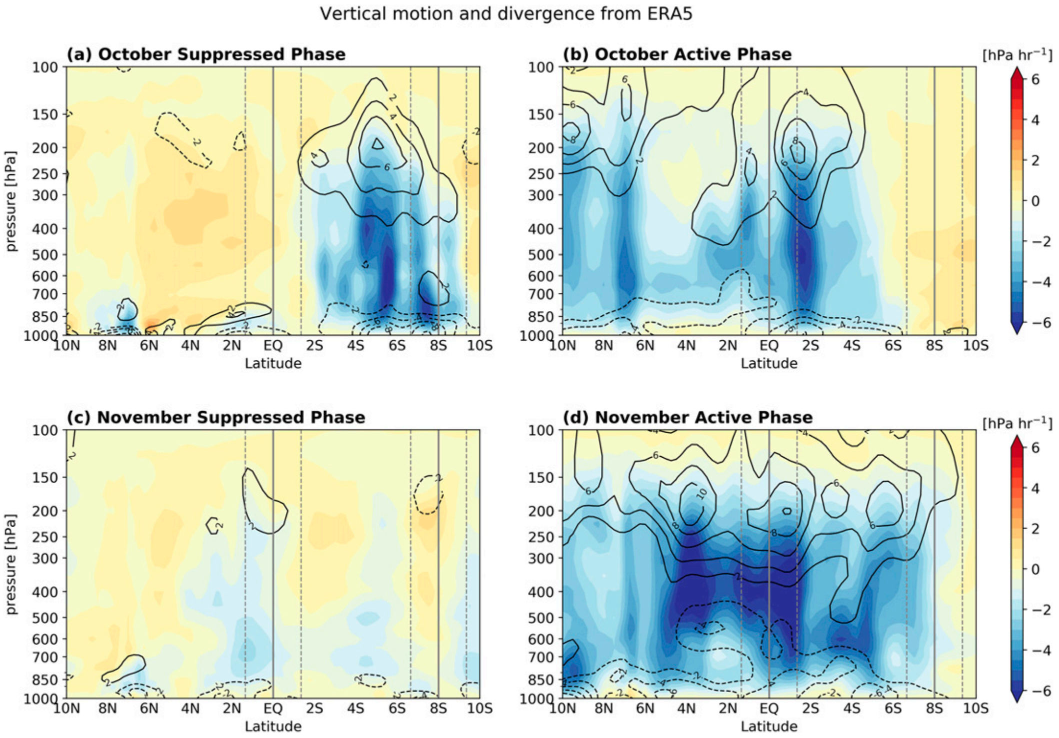

FIG. 3. Latitudinal cross section of vertical motion (shaded, $\mathrm{hPa\,h^{-1}}$) and divergence (contoured, $10^{-6}\,\mathrm{s^{-1}}$) from ERA5 averaged longitudinally across the radar volume and across times associated with the (a) October suppressed phase, (b) October active phase, (c) November suppressed phase, and (d) November active phase. Solid vertical lines mark the locations of the *Revelle* (EQ) and *Mirai* (8°S) while dashed lines mark the edge of the radar volumes.

ITCZ band, convergence was maximized at $-10^{-5}\,\mathrm{s^{-1}}$, and divergence reached a maximum aloft around 200 hPa. These results are consistent with those from Ciesielski et al. (2018), despite the difference in datasets used (ERA5 in this study vs interpolated sounding data in Ciesielski et al. 2018). As the MJO entered the active period, the maximum in upward motion shifted north toward the equator, maximizing near 2°S at $-6\,\mathrm{hPa\,h^{-1}}$ (Fig. 3b). At this time, the location of the *Mirai* was subjected to subsidence.

The environment following the first MJO was characterized by a weak circulation within the central IO (Fig. 3c). There was no strong vertical motion observed at the *Revelle* or *Mirai*, and only small pockets of surface convergence were evident. As the second MJO became more pronounced, vertical motion significantly increased throughout the region and was considerably more widespread than the first MJO active period (Fig. 3d). Strong upward motion ($>-6\,\mathrm{hPa\,h^{-1}}$) was seen over the entire *Revelle* radar domain and toward the north around 4°N, while vertical motion and surface convergence remained limited around the *Mirai*.

a. Revelle *results*

A *Revelle* time series of atmospheric parameters including lapse rate and relative humidity (RH) profiles for each MJO is shown in Fig. 4. The lapse rate profiles (Fig. 4a) depict three stable layers ($-dT/dz < 5\,\mathrm{K\,km^{-1}}$), consistent with results from Johnson et al. (1996, 1999): the trade wind–like inversion, the 0°C level, and the tropopause. Both MJOs exhibited a stable layer around 800 hPa that resembled the trade wind inversion prevalent in the tropics. This inversion is largely due to large-scale subsidence from the Hadley and Walker circulations but can be modulated by local processes including radiation and convection (Yu et al. 2018). This stable layer, along with the tropopause near 125 hPa, can act to inhibit cloud growth and thus contribute to the distribution of PF types. A weaker stable layer was also evident around 550 hPa which closely aligned with the 0°C level. As shown in Johnson et al. (1996), this stable layer was likely due to hydrometeor melting and resultant cooling associated with large stratiform rain areas. Therefore, this stable layer did not impact the distribution of PFs, but rather was a result of PFs, most notably, the presence of deep convection which produced stratiform precipitation. This stable layer was especially strong in the active phase of MJO2 which contained significant stratiform rain areas (Fig. 4d). As commented by Johnson et al. (1996) and evident in Fig. 4d, such stable layers can persist after the deep convection and stratiform precipitation dissipates.

During the suppressed phases, there was considerable dry air above the 0°C level, especially during MJO1 ($\mathrm{RH} < 50\%$; Fig. 4b). This, along with drier air below the 0°C level, acted to impede convection, and as a result, the suppressed phases were dominated by isolated PFs that produced small amounts of rain (Figs. 4c,d). As the MJO moved across the IO, the troposphere began to moisten (due to an increase in moderately deep

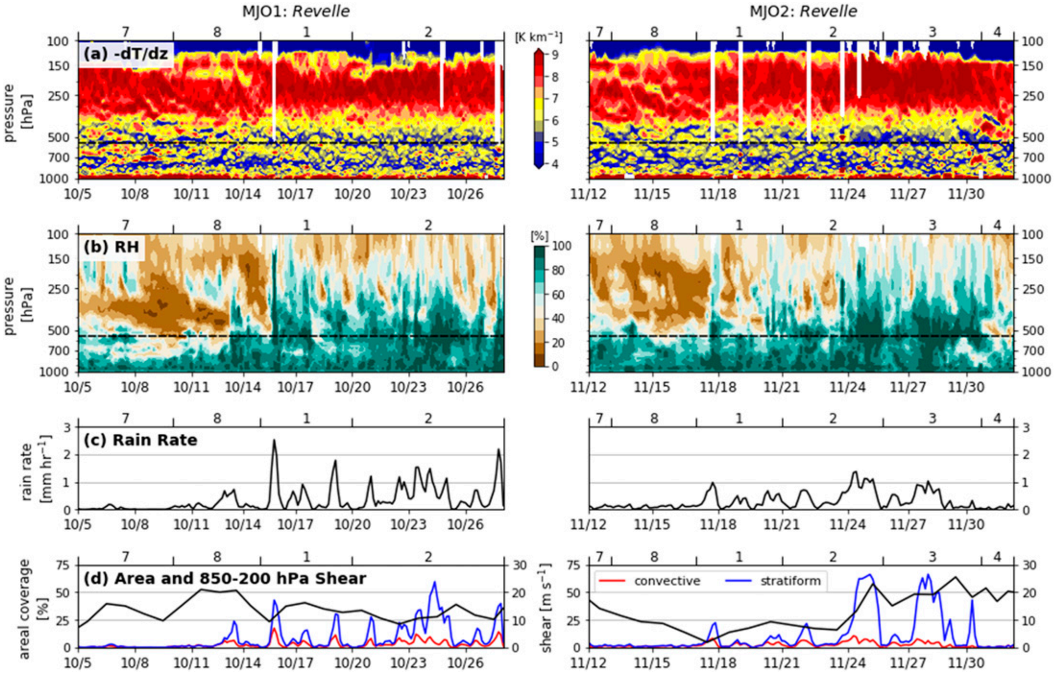

FIG. 4. Time series from MJO1 and MJO2 of the *Revelle*. (a) Lapse rate profiles (K km^{-1}), (b) relative humidity profiles (%), (c) areal mean rain rate (mm h^{-1}), and (d) percent of total domain associated with convective (red) and stratiform (blue) rain from radar PFs and 850–200 hPa wind shear (black, m s^{-1}). Dashed black line in (a) and (b) represents approximate height of 0°C isotherm. WH MJO phases shown on the top axes.

convection; Powell and Houze 2015; Takemi 2015; Xu and Rutledge 2016; Powell 2016), which created a favorable environment for mesoscale systems to develop and persist (Fig. 4b). Areal mean rain rates during both MJOs were highest during the active phases, with MJO1 exhibiting more episodic events that were shorter and more intense compared to MJO2 (Fig. 4c). This relates back to the large-scale vertical motion which was more widespread during MJO2 compared to MJO1 (Figs. 3b,d). There was significantly more stratiform area associated with mesoscale events during the active phase of MJO2 (~75% of the domain), which lowered the areal mean rain rates (Figs. 4c,d). These larger stratiform events coincided with an increase in deep tropospheric shear (850–200 hPa; Fig. 4d), which likely acted to distribute ice particles detrained from deep convection (Houze 2004; Yamada et al. 2010). Additionally, two westerly wind bursts (WWB) were observed during the active phase of MJO2 (Moum et al. 2014; Thompson et al. 2018), which were characterized by sustained surface winds > 7 m s^{-1} for more than 24 h (Harrison and Vecchi 1997; Thompson et al. 2018). These WWBs were also associated with a significant increase in boundary layer convergence ($>-10^{-4}$ s^{-1}; Fig. 5) and the generation of shallow convection. This shallow convection then dissipated into widespread stratiform precipitation and likely contributed to the enhancement in stratiform area during these time periods.

b. Mirai *results*

A similar analysis was performed at the *Mirai* for both MJOs. The lapse rate profile over the *Mirai* was considerably different from the *Revelle* (Fig. 6a). The trade wind–like inversion was more defined at the *Mirai*, with low-level lapse rates ~2 K km^{-1} lower on average compared to lapse rates observed over the *Revelle*. This increased stability could have been caused by overall weaker convection that disrupted the stable layer less so compared to intense convection. This weaker convection may be partially explained by the extremely dry air (<20% RH) within the midlevels during the majority of both MJO events (Fig. 6b). These dry-air intrusions from the subtropics (similar to ones observed during TOGA COARE; DeMott and Rutledge 1998) acted to suppress convection within the ITCZ, located south of the equator near the *Mirai* (Fig. 3), especially leading up to MJO2 (Kerns and Chen 2014). ITCZ-induced subsidence over the equator was then reduced, which caused an equatorward shift in precipitation, and may have aided in the initiation of MJO2 (Fig. 3; Kerns and Chen 2014). A recent study by Zelinsky et al. (2019) showed that the ITCZ was not a necessary feature for MJO initiation but could impact the large-scale circulation and moisture field to make conditions favorable for MJO initiation.

In addition to the stronger trade wind–like inversion, there was no prominent stable layer at the 0°C level, consistent with the near absence of large stratiform rain events (Figs. 6a,d). In agreement with Xu et al. (2015), large rain events were much less frequent, weaker when they were present, and did not occur in specific phases like at the *Revelle* (Fig. 6c). Around the *Mirai*, the largest rain event in MJO1 occurred in the suppressed phase and had similar characteristics as the largest event in MJO2, which occurred during the active phase, with

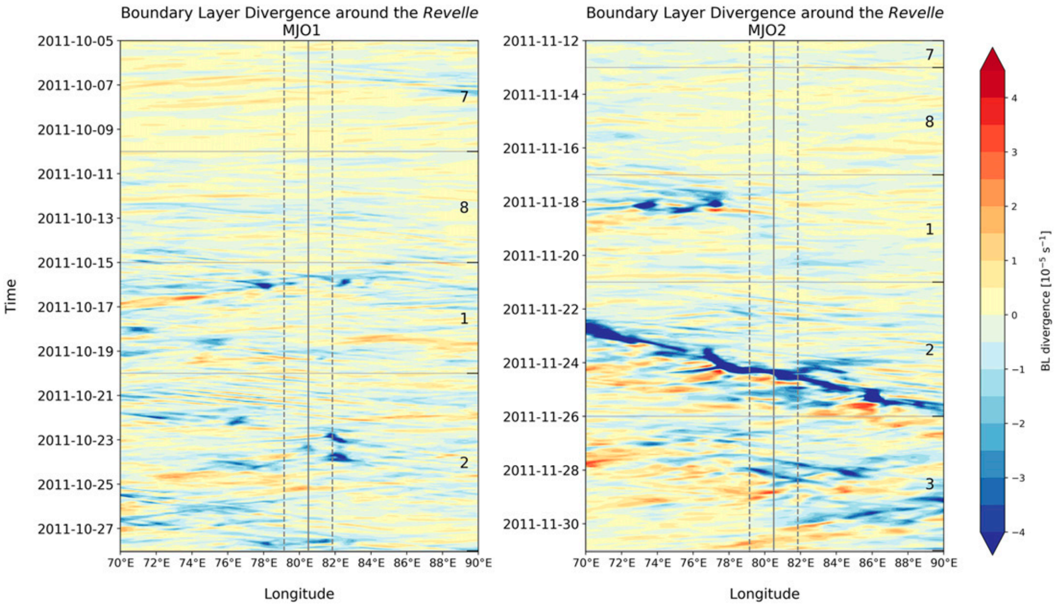

FIG. 5. Time–longitude diagram of mean 1000–800 hPa divergence (10^{-5} s^{-1}) from ERA5, averaged latitudinally around the *Revelle*. Solid vertical line marks the *Revelle* location while dashed lines mark the edge of the radar volume. WH MJO phases shown on the right axes.

roughly 40%–50% of the domain associated with stratiform precipitation (Fig. 6d). Consistent with results from the *Revelle*, stratiform area was enhanced in the presence of stronger deep tropospheric wind shear (Fig. 6d). However, around the *Mirai*, there was less stratiform area associated with mesoscale rain events compared to around the *Revelle*. This agrees with Lin et al. (2004), who found that higher percentages of stratiform rain were associated with the MJO compared to the global tropical mean.

4. PF statistics

It is important to first consider how the morphology of PFs vary between phases of the MJO before examining the DC

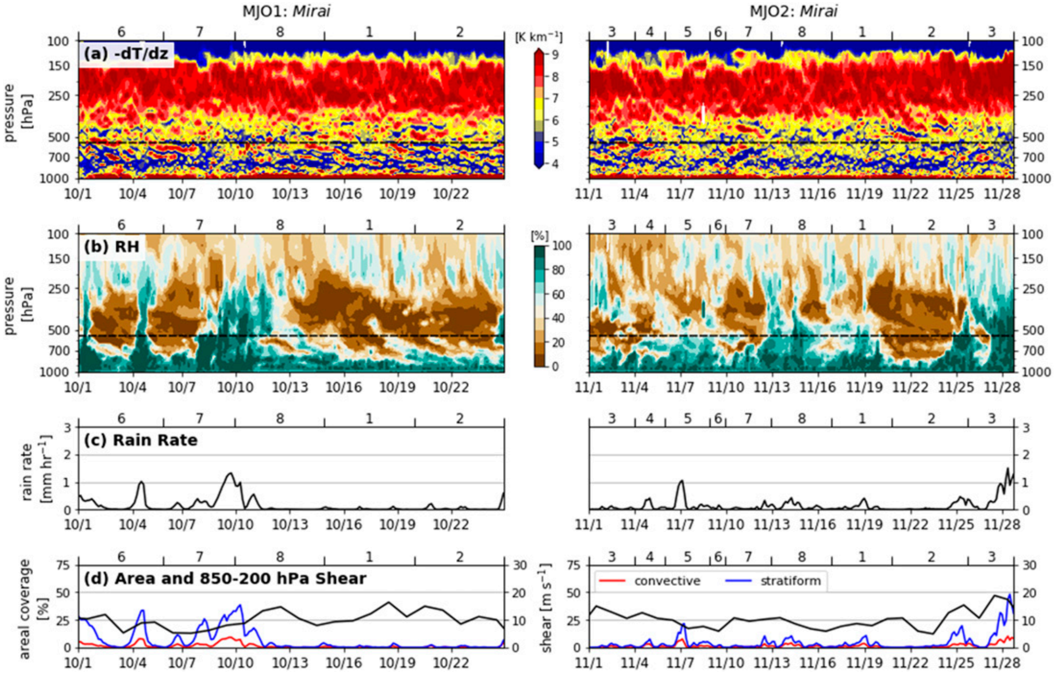

FIG. 6. As in Fig. 4, but for the *Mirai*. Note different dates and WH phases.

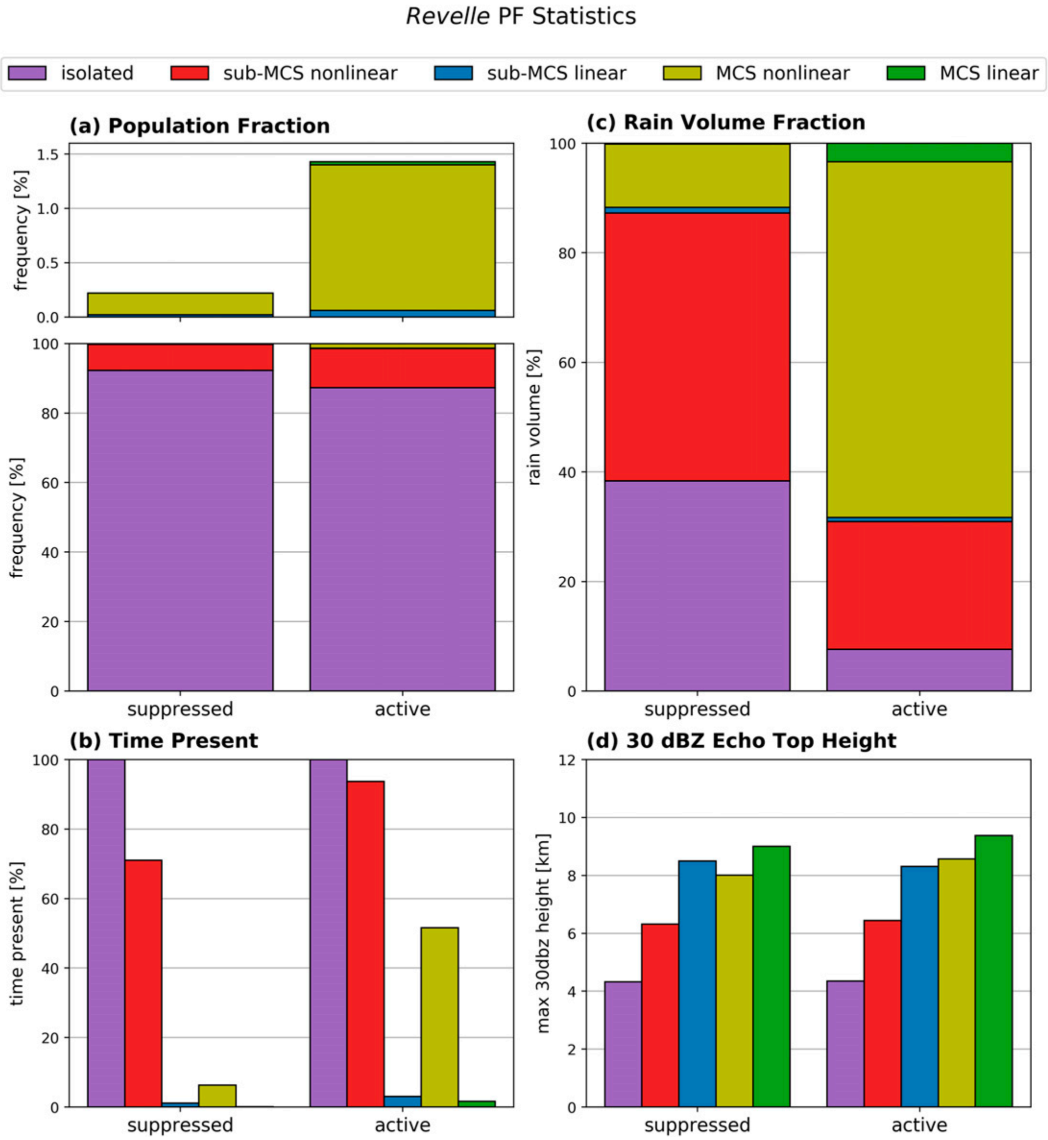

FIG. 7. PF rain statistics by phase and morphology from the *Revelle*. (a),(bottom) Fraction of the population and (a),(top) zoomed in on MCS nonlinear PFs, (b) percent of the time present, (c) rain volume fraction, and (d) 30-dBZ convective echo-top height (km).

of PFs. The goal here is to be able to relate changes in rain statistics from individual PF categories to changes in environmental parameters to understand some of the processes that control PF type, especially linked to interactions between the ocean and atmosphere.

a. Revelle *results*

Rain statistics including percent of total population, time present, rain volume contribution, and 30-dBZ convective echo-top heights for each of the five PF morphologies documented by the *Revelle* C-band radar are shown in Fig. 7 for the suppressed and active phases. Isolated features dominated the frequency distribution, with sub-MCS nonlinear events a distant second (Fig. 7a). Sub-MCS linear, MCS nonlinear, and MCS linear events represented the remaining ~2% of the population. Isolated PFs were observed in nearly every radar volume scan, while sub-MCS nonlinear events were present on average 82% of the time (Fig. 7b). However, the likelihood of a sub-MCS nonlinear event being identified during the active phase was higher (more than 90%) than during the suppressed phase (~70%). A substantial reduction in the total precipitable water (significant at the 95% confidence level) was observed during the suppressed phase (average of 50 mm) compared to the active phase (average of 59 mm), which likely played a role in suppressing convection (Fig. 8a). Additionally, the average surface moisture, SST, and sensible heat flux were lower during the suppressed phase (Figs. 8b,c,f), all of which created a less-than-favorable environment for larger convective systems to develop.

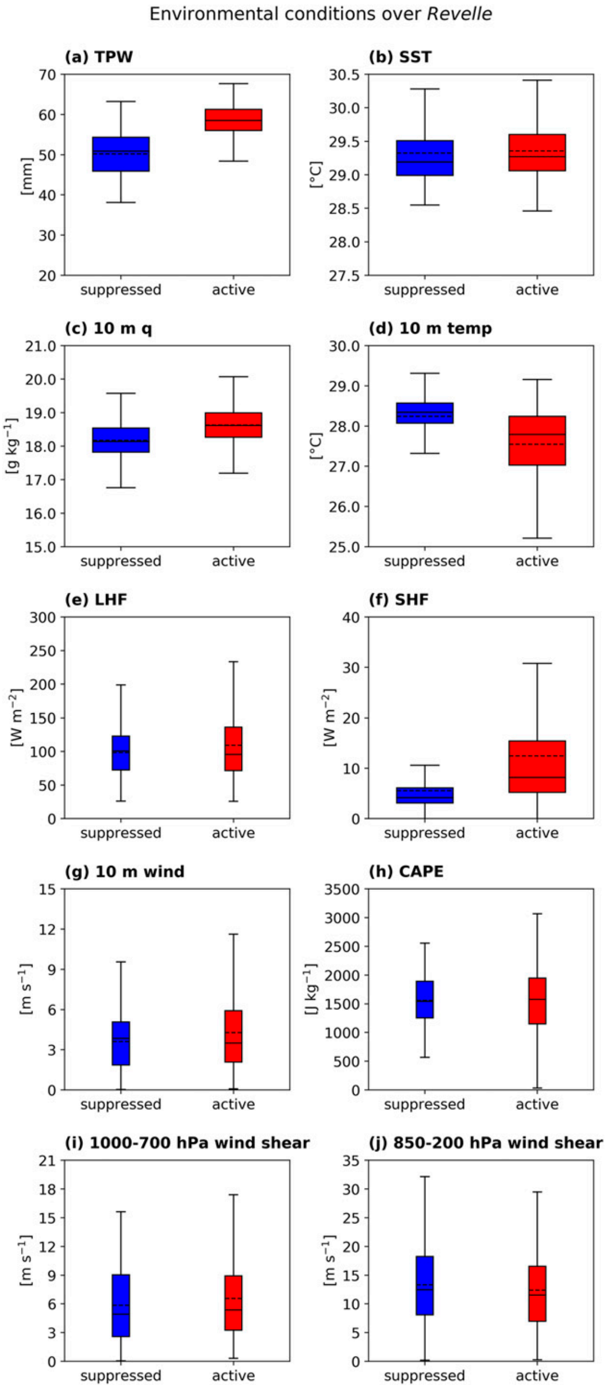

FIG. 8. Boxplots of environmental conditions observed at the *Revelle* during the suppressed (blue) and active (red) phases. (a) Total precipitable water (mm), (b) SST (°C), (c) 10 m specific humidity (g $\mathrm{kg^{-1}}$), (d) 10 m temperature (°C), (e) latent heat flux (W $\mathrm{m^{-2}}$), (f) sensible heat flux (W $\mathrm{m^{-2}}$), (g) 10 m wind (m $\mathrm{s^{-1}}$), (h) CAPE (J $\mathrm{kg^{-1}}$), (i) 1000–700 hPa wind shear (m $\mathrm{s^{-1}}$), and (j) 850–200 hPa wind shear (m $\mathrm{s^{-1}}$). The solid (dashed) line represents the median (mean), the box spans the lower and upper quartiles of the data, and the whiskers extend to 1.5 times the interquartile range. Wider boxplots show parameters whose suppressed and active phase medians are significantly different at the 95% confidence level (according to the binomial test).

MCS nonlinear events occurred predominately during the active phase with about half of all radar volume scans in this phase group having an MCS nonlinear event (Fig. 7b). The percent of rain volume contribution from MCS nonlinear events was significantly different between the suppressed (~10%) and active phases (~65%; Fig. 7c). The active phase was marked by higher precipitable water and stronger sensible heat flux on average (Figs. 8a,f). Additionally, stronger latent heat fluxes were more likely to occur during the active phase (Fig. 8e). Several studies have shown that convection can enhance air–sea fluxes through processes including convective outflows, which work to enhance surface winds and reduce near-surface temperatures (Johnson and Nicholls 1983; Jabouille et al. 1996; Saxen and Rutledge 1998; Yokoi and Yoneyama 2014). The enhancement of sensible heat flux during the active phase due to near-surface temperature reduction (Fig. 8d; significant at the 95% confidence level) and near-surface wind enhancement (Fig. 8g) was evident at the *Revelle*.

The PF convective 30-dB*Z* echo-top heights increased with increasing size and degree of linear organization of PFs (i.e., the convective cores of linear events were deeper than those of nonlinear events within each PF size; Fig. 7d). Isolated features had average peak heights near 4.3 km MSL, just below the freezing level, suggesting the vast majority of these echoes were governed by warm rain processes. MCS linear events had convective heights on average around 9.2 km MSL, about 1 km higher than MCS nonlinear events. In fact, rain rates were generally higher within individual linear systems (not shown) compared to nonlinear systems. One hypothesis for these differences is the so-called RKW theory (Rotunno et al. 1988; Weisman et al. 1988) in which vorticity generated by the advancing cold pool is balanced by the environmental shear. When this happens, the deepest lifting occurs along the leading edge and convection is enhanced (Weisman and Rotunno 2004). However, idealized simulations of tropical convection by Grant et al. (2018) suggest that gravity waves may be more important in determining mesoscale organization. It is important to point out that the sample size of linear features was considerably lower than isolated and nonlinear features (Table 1), and thus it would be interesting to see whether a similar trend in echo-top heights is seen in larger datasets, for example, a TRMM (GPM)-based climatology.

In addition to differences in convective echo tops between PF morphologies, there were small variations in heights between phases, with heights being slightly larger during the active phase compared to the suppressed phase. There were no significant differences in CAPE between the two phases, although the range of CAPE was larger during the active phase, consistent with the life cycle of mesoscale systems (Fig. 8h). The greatest lower tropospheric wind shear values occurred during the active phase, which could have played a role in the increased echo-top heights (consistent with RKW theory; Fig. 8i). This increase in echo-top heights observed during the active phase is consistent with the analysis from Xu and Rutledge (2014), who found the frequency of deep, intense convection was maximized in phase 1.

b. Mirai *results*

A similar analysis was performed at the *Mirai*. Like at the *Revelle*, isolated PFs again accounted for a large fraction of the

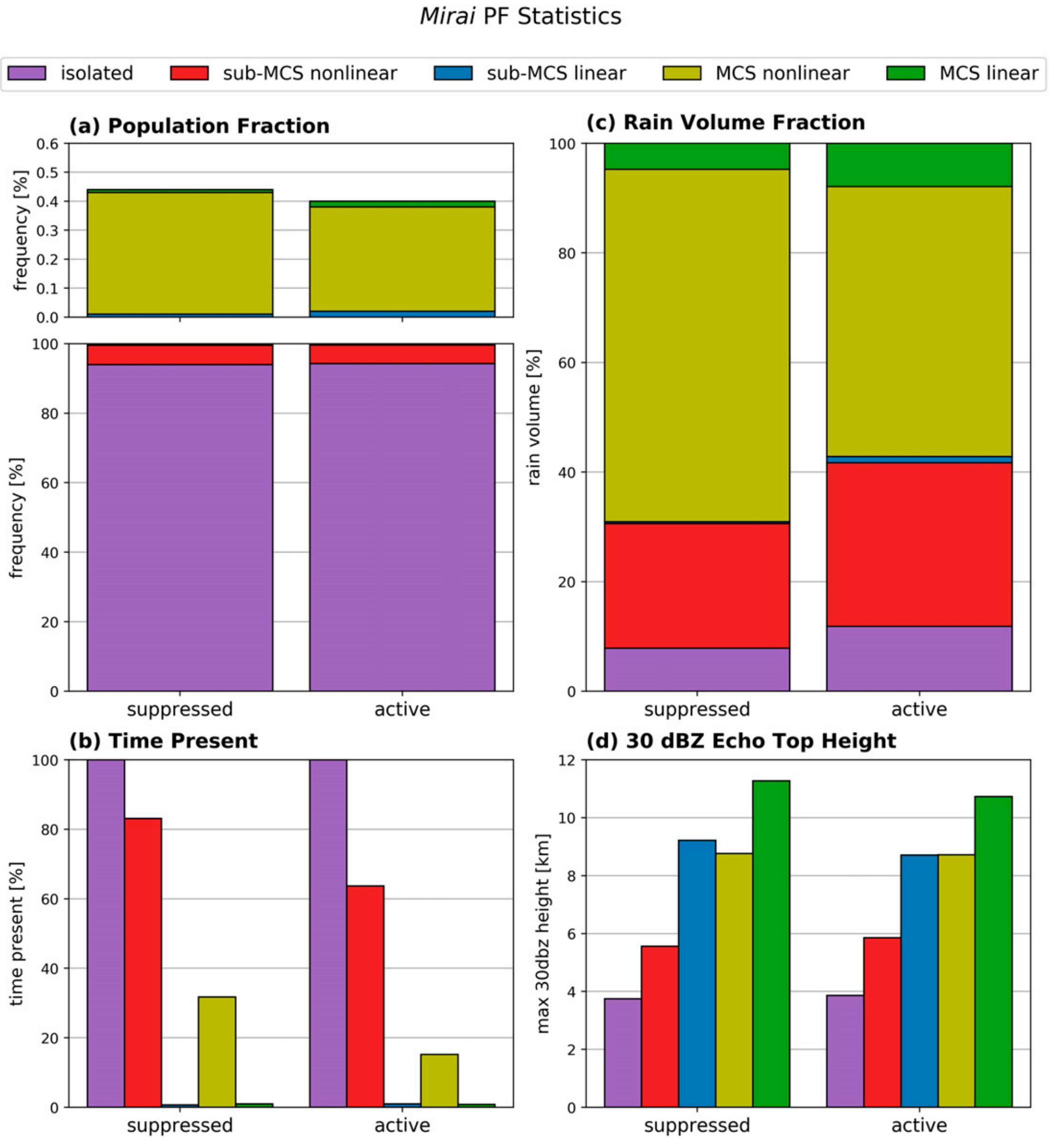

FIG. 9. As in Fig. 7, but for the *Mirai*.

PFs observed at 94% (90% at the *Revelle*; Fig. 9a). Sub-MCS nonlinear events occurred more often during the suppressed phase, opposite from the results at the *Revelle* (Fig. 9b). MCS nonlinear events were observed 30% of the time during the active phase and 15% of the time during the suppressed phase. This increase in the number of features agrees with Xu et al. (2015), who found deeper convection developed off-equator when conditions were suppressed along the equator. Total precipitable water was significantly higher on average during the suppressed phase (47 mm) compared to the active phase (42 mm; Fig. 10a). SSTs did not vary much throughout the field campaign, but were greater during the suppressed phase (significant at the 95% confidence level; Fig. 10b). Air–sea fluxes were also enhanced during the suppressed phase at the *Mirai*, primarily due to increased surface winds and reduced temperatures (Figs. 10d,e,f,g).

Isolated features contributed significantly less to the total rain volume at the *Mirai* compared to the *Revelle*, especially during the suppressed phase (Fig. 9c). However, there was not a large difference in the PF rain volume contributions between suppressed and active phases at the *Mirai*. MCS nonlinear events accounted for ~65% of the total rain volume during the suppressed phase and ~50% of the total rain volume during the active phase. The range of CAPE was larger in the presence of enhanced MCS activity, although CAPE was much lower than at the *Revelle* on average (about 50% reduced, primarily due to drier and slightly cooler surface conditions; Figs. 10c,d,h). Convective 30-dBZ echo-top heights similarly increased with increasing size and degree of organization like at the *Revelle*, and echo tops were typically highest in the suppressed phase (Fig. 9d). The low-level wind shear observed at the *Mirai* was larger than at the *Revelle*, primarily

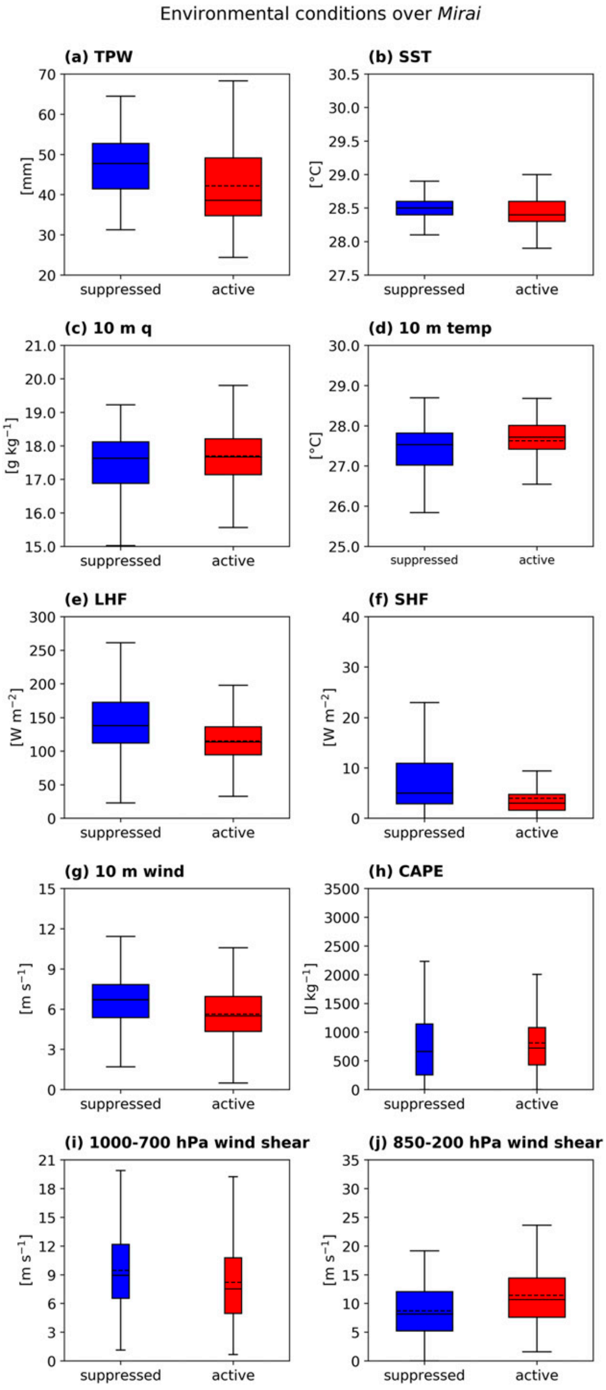

FIG. 10. As in Fig. 8, but for the *Mirai*.

due to increased surface winds (Figs. 10g,i). In fact, average surface wind speeds observed at the *Mirai* were nearly 50% greater than those observed at the *Revelle*. The deep layer wind shear was reduced at the *Mirai* during both phases compared to the *Revelle*, which may have played a role in constraining the size of any mesoscale systems that did develop (Fig. 10j).

5. DC of PFs

This section aims to describe the evolution of precipitation and convective organization over the course of the DC and how these quantities vary during suppressed and active MJO periods both on- and off-equator in the central IO. Similar studies have investigated how PFs evolve within active periods of the MJO (i.e., growth of deep convective cores to broad stratiform regions; Zuluaga and Houze 2013; Rowe et al. 2019), but these DYNAMO studies did not evaluate how convective organization is related to the DC of rainfall, nor did they consider the off-equator location and the contrast that location offers relative to the on-equator location.

a. Revelle *results*

The DC of the frequency and areal mean rain rates for all PFs as a function of time of day and phase group at the *Revelle* is shown in Fig. 11. The frequency represents the percentage of PFs found during any given hour. The diurnal variability of the frequency of events in the active phase was smaller than in the suppressed phase, and a frequency maximum was achieved between 0000 and 0300 LT during the suppressed phase (Fig. 11a).

There were large differences in the areal mean rain rates during the suppressed and active phases at the *Revelle* (Fig. 11b). Rain rates were much larger, averaging ~11 mm day^{-1} during the active phase and only ~2.5 mm day^{-1} during the suppressed phase. The DC showed an increase in rain rates from 1300 LT to a maximum at 0100 LT during the active phase with a range of about 6 mm day^{-1}. The DC during the suppressed phase was not as strong, with two local maxima occurring around 1500 and 0100 LT and a range of about 1 mm day^{-1}.

The convective rain fraction was higher on average during the suppressed phase at 90%–95%, but there was little diurnal variation (Fig. 11c). There was more variability during the active phase though, with an increase in convective rain fraction from ~75% to ~80% in the afternoon. The stratiform fraction was highest during the active phase, averaging around 20% and consistent with greater MCS activity (Fig. 11d). These results generally agree with Thompson et al. (2015), who found the average convective/stratiform rain fraction over the tropical IO was 80/20 (derived from disdrometer data opposed to radar observations here).

To investigate how individual PF morphologies contributed to the total rain rates and frequency, the DCs of rain volume fraction of each PF type were analyzed. During the suppressed phase, isolated and sub-MCS nonlinear events contributed the most to the total rain volume at any given time (Fig. 12a). Isolated features peaked in average rain volume contribution at 1200 LT, after which the rain volume fraction for sub-MCS nonlinear features began to increase throughout the evening and early morning hours. Sub-MCS nonlinear events represented ~40% of the total rain volume on average by 0500 LT. MCS nonlinear rain volume fraction peaked at 1500 LT and again at 0000 LT consistent with the afternoon and early morning maxima in rain rates (Fig. 11b). During the active phase, MCS nonlinear rain volume contribution increased after 1500 LT until the next morning where it reached peak

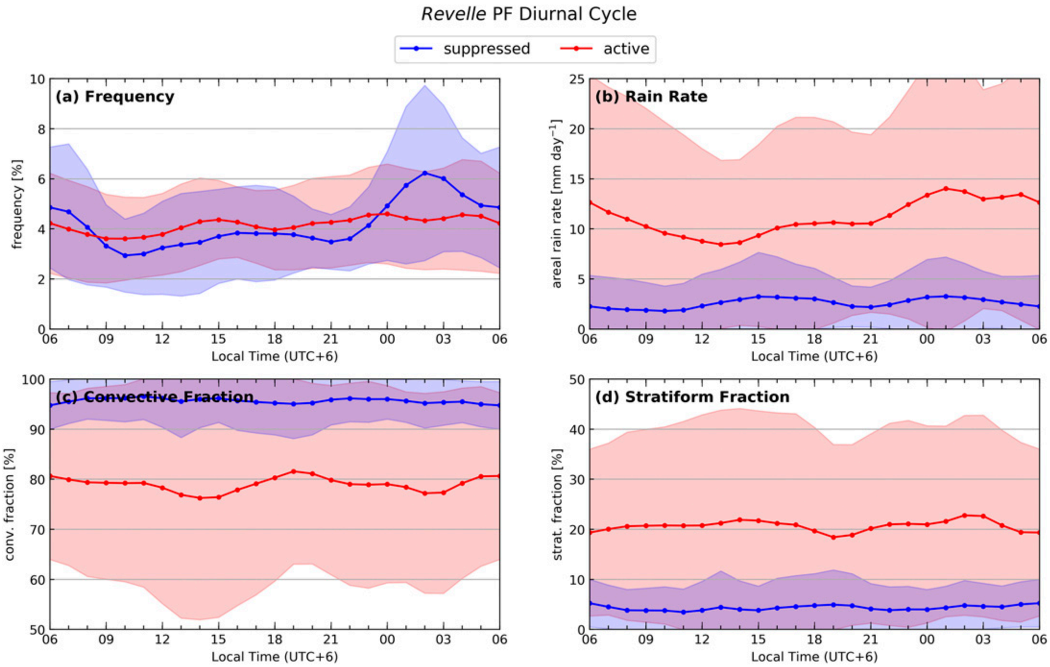

FIG. 11. Diurnal cycle of (a) frequency, (b) areal mean rain rate, (c) convective rain fraction, and (d) stratiform rain fraction from *Revelle* PFs for suppressed (blue) and active (red) phases. Shaded areas represent one standard deviation above and below the mean; 1–2–1 triangular smoothing was applied to each group.

values at around 50% at 0200 LT (Fig. 12b). This rain volume distribution was most similar to the DC of rain rates observed in Fig. 11b. Additionally, upon further analysis it was found that the rain volume of MCS nonlinear features during the active phase was significantly larger compared to the suppressed phase (not shown). Sub-MCS nonlinear features appeared to dominate the DC of rainfall during the suppressed phase, while MCS nonlinear features governed the DC during the active phase. During both phases, linear events did not have a significant contribution since they occurred at very low frequency.

To analyze how the DC of PFs was related to the environment, profiles of RH, vertical motion, and divergence as a function of time are shown in Fig. 13. During the suppressed phase, there was dry air (RH < 50%) above the 0°C level which did not vary much throughout the day (Fig. 13a). Below the 0°C

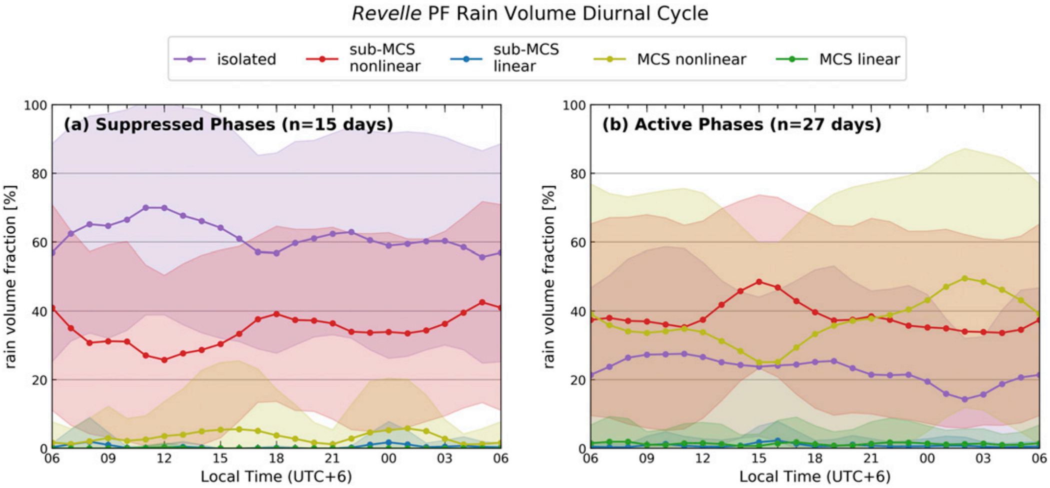

FIG. 12. Diurnal cycle of rain volume fractions for each PF morphology at the *Revelle* during the (a) suppressed and (b) active phases. Shaded areas represent one standard deviation above and below the mean; 1–2–1 triangular smoothing was applied to each group.

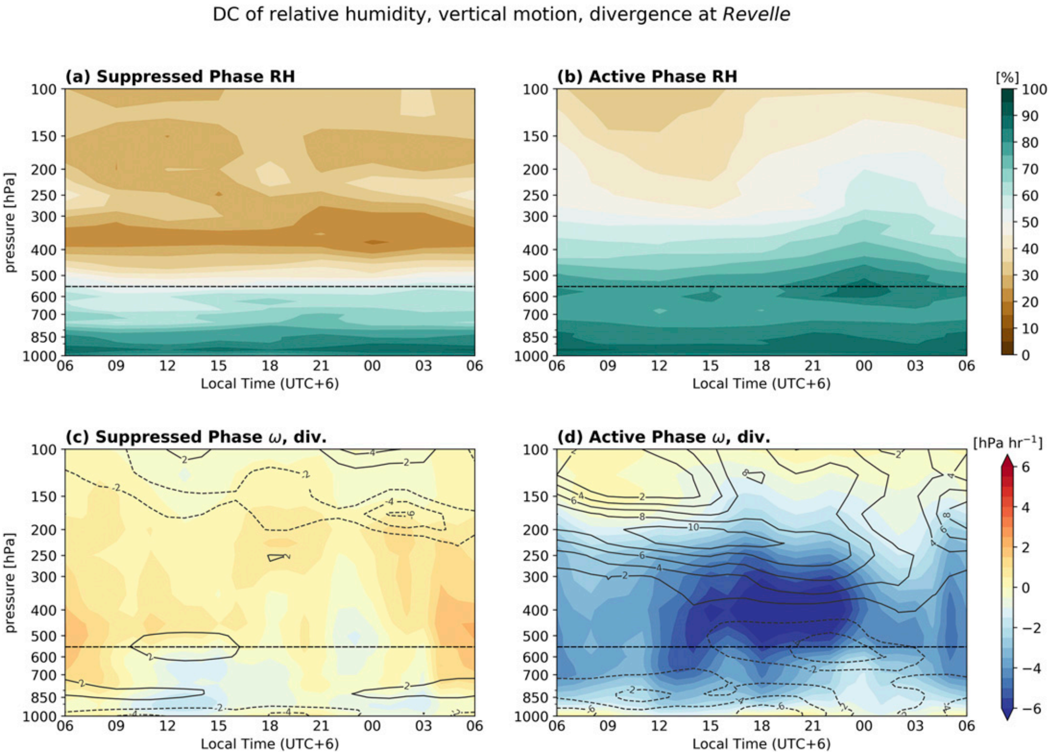

FIG. 13. Diurnal cycle of relative humidity during (a) suppressed and (b) active phases. (c),(d) As in (a) and (b), but showing vertical motion (shaded, hPa h^{-1}) and divergence (contoured, 10^{-6} s^{-1}) from ERA5, averaged within the *Revelle* radar volume. Dashed black line represents approximate height of 0°C isotherm.

level, moist air (RH > 80%) was mainly contained within the boundary layer, and RH slightly increased overnight. In contrast, the column was moister during the active phase, with the maximum RH achieved at midnight at the surface and around the 0°C level, consistent with mesoscale activity (Figs. 12b, 13b).

Looking at vertical motion and divergence during the suppressed phase, there was very little upward motion throughout the day, with subsidence dominating the region (Fig. 13c). This was consistent with the large-scale average subsidence observed at the *Revelle* (Fig. 3). Additionally, there was only weak surface convergence which was observed around 1800 LT. During the active phase, there was very strong upward motion all day, which maximized around 400 hPa between 1800 and 2100 LT (>-6 hPa h^{-1}; Fig. 13d). Coinciding with this maximum was the maximum in convergence at the surface (-6×10^{-6} s^{-1}). A secondary maximum in convergence was observed around the 0°C level between 2100 and 0000 LT. During this time, rain rates were enhanced, and MCS nonlinear rain volume fraction was increasing (Figs. 11b, 12b).

An analysis of the DC of surface environmental parameters including SST, CAPE, and air–sea fluxes is shown in Fig. 14. During both phases, SST peaked around 1400 LT (Fig. 14a), about 2 h after the peak in local solar heating (Fig. 14b). These peaks in SST and solar heating were statistically significant. The amplitude of SST was stronger in the suppressed phase compared to the active phase. A reduction in solar heating due to increased MCS activity (Fig. 14b) and a slight increase in average surface winds during the active phase (Fig. 14c) prevented diurnal warm layers from forming (Thompson et al. 2018) and likely drove the weaker DC in SST. The diurnal range of CAPE was about 500 J kg^{-1}, which peaked around midnight (Fig. 14d). This peak in CAPE around 0000 LT was statistically significant during the suppressed phase and matched the variation in surface dewpoint temperatures (not shown), which was likely driven by cumulus moistening and air–sea fluxes (Sui et al. 1997; Ruppert and Johnson 2015; Sakaeda et al. 2018). A similar CAPE DC was found during TOGA COARE (Petersen et al. 1996) and the *Mirai* Indian Ocean Cruise for the Study of the MJO-Convection Onset experiment (MISMO; Bellenger et al. 2010). Bellenger et al. (2010) suggested CAPE remains high overnight due to radiational cooling in the mid- to upper troposphere.

Both latent and sensible heat fluxes showed some degree of diurnal variability between phases. Latent heat flux was very similar between phases during the morning and early afternoon hours, reaching a single peak 1600–1700 LT (Fig. 14e). Latent heat flux then decreased more gradually on average during the active phase compared to the suppressed phase. This difference was most likely due to the difference in Δq between the two phases (Fig. 14f). The DC of Δq was larger during the suppressed phase compared to the active phase (although Δq differences between 1200 and 0000 LT were statistically significant in both phases), and there was a sharper decrease in the

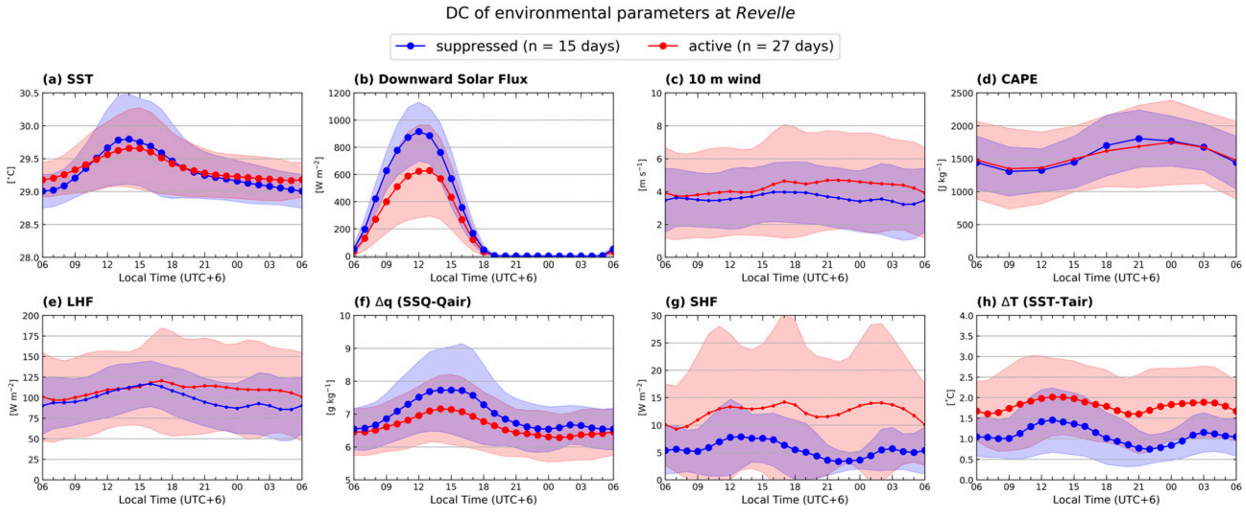

FIG. 14. Diurnal cycle of environmental parameters from the *Revelle* during suppressed (blue) and active (red) phases. (a) SST (°C), (b) downward solar flux (W m^{-2}), (c) 10 m wind speeds (m s^{-1}), (d) CAPE (J kg^{-1}), (e) latent heat flux (W m^{-2}), (f) Δq (SSq − q_{air}; g kg^{-1}), (g) sensible heat flux (W m^{-2}), and (h) ΔT (SST − T_{air}; °C). Shaded areas represent one standard deviation above and below the mean. Larger markers indicate the medians of each parameter at local noon and midnight are significantly different at the 95% confidence level (according to the binomial test); 1–2–1 triangular smoothing was applied to each group.

afternoon. Sensible heat flux varied more between the suppressed and active phases and showed a more bimodal DC (Fig. 14g). Sensible heat flux was higher on average during the active phase and reached maxima in the afternoon and just after midnight. The DC of sensible heat flux correlated well with the DC of ΔT, with the afternoon peak corresponding to the peak SST, and the smaller early morning peak due to a sharper decrease in T_{air} (Fig. 14h). JC13 found a similar near-surface cool anomaly over the northern sounding array during the active phase which they attributed to precipitation and convective downdrafts. A similar DC was observed during the suppressed phase, although the morning peak was not as significant, consistent with a weaker DC in ΔT.

b. Mirai *results*

The DC of precipitation, convective organization, and environmental parameters was significantly different at the *Mirai* compared to the *Revelle*. The DC of the frequency of PFs exhibited a single peak in the early morning hours (Fig. 15a). The DC of rain rates during the suppressed phase was weak, with values holding steady at around 6 mm day^{-1} (Fig. 15b). During the active phase, the rain rate distribution was bimodal, with peaks occurring at 1500 and 0100 LT, consistent with the suppressed phase at the *Revelle*. However, the rain rates were much lower than what was observed at the *Revelle*, with the two maxima reaching only about 4 mm day^{-1}. In addition, the convective and stratiform rain fractions for both phases were fairly similar, with convective rain representing 80%–90% of the total rain volume, and stratiform representing the remaining 10%–20% (Figs. 15c,d).

The DC of PF rain volume fraction also varied between suppressed and active phases at the *Mirai* (Fig. 16). During the suppressed phase, isolated features contributed the most to the total rain volume on average around 1200 LT (40%; Fig. 16a). After 1200 LT, sub-MCS nonlinear features began to increase in rain volume fraction, while MCS nonlinear features began to decrease. MCS nonlinear features then began to increase in rain volume fraction near 2100 LT and reached peak contributions at sunrise (consistent with results from Ciesielski et al. 2018). The DC of rain volume fraction during the active phase at the *Mirai* was similar to the suppressed phase at the *Revelle* (Fig. 16b). Isolated features contributed the most to the total rain volume, followed by sub-MCS nonlinear features and MCS nonlinear features. Isolated features peaked in the late morning hours, after which sub-MCS nonlinear features began to increase in rain volume contribution. MCS nonlinear features contributed <10% on average to the rain volume throughout the day, although there was a slight increase observed just after midnight, consistent with an increase in rain rates (Fig. 15b). Similar to the *Revelle*, linear features did not contribute much to the total rain volume in either phase at the *Mirai*.

The DC of RH, vertical motion, and divergence averaged around the *Mirai* is shown in Fig. 17. The RH profiles look similar between the active and suppressed phases. Moist air was limited to below 700 hPa in the suppressed phase (Fig. 17a), and within the boundary layer during the active phase (Fig. 17b). There was little variability throughout the day in low-level RH. Above the 0°C level, the driest air occurred overnight during the suppressed phase and during the day for the active phase. Overall, the column was drier throughout the day during the active phase, consistent with reduced total precipitable water (Fig. 10a).

One noticeable difference between the *Revelle* and *Mirai* environments was the lack of strong upward motion around the *Mirai*. The suppressed phase was characterized by weak upward motion which increased in height from around 800 hPa at 0900–1200 LT to 450 hPa at 1200–1500 LT (Fig. 17c).

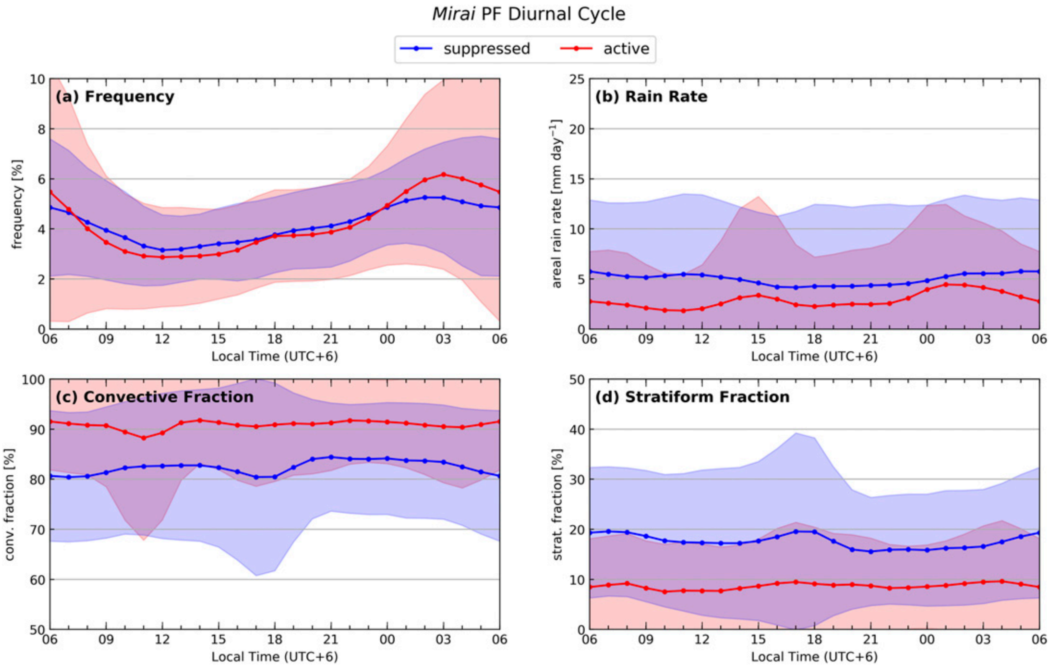

FIG. 15. As in Fig. 11, but for the *Mirai*.

This similar pattern was also observed starting at midnight. Ciesielski et al. (2018) found the maximum vertical motion within the ITCZ occurred 0500–0800 LT during the October suppressed period. However, from the large-scale vertical motion observed in Fig. 3, the majority of the vertical motion is located north of the *Mirai*'s location. Additionally, the November suppressed period exhibited weak vertical motion, so averaging both suppressed periods provides a different result than Ciesielski et al. (2018). The strongest divergence during the suppressed phase occurred 1800–2100 LT, corresponding to an increase in the sub-MCS nonlinear rain volume fraction (Fig. 16a). During the active phase, there was very little upward vertical motion observed across the *Mirai*, and there was no surface level convergence (Fig. 17d). This was most similar to the suppressed phase at the *Revelle* and highlights the lack of deep convection in the area.

Looking into the environmental parameters (Fig. 18), one noticeable result is that the variability between phases at the *Mirai* was much less than compared to the *Revelle*. The DC of SST was strongly damped, and SSTs were on average 0.5°–1°C cooler than at the *Revelle* (Fig. 18a). There was not a large difference between the solar flux observed during the suppressed and active phases (Fig. 18b). Surface winds were higher

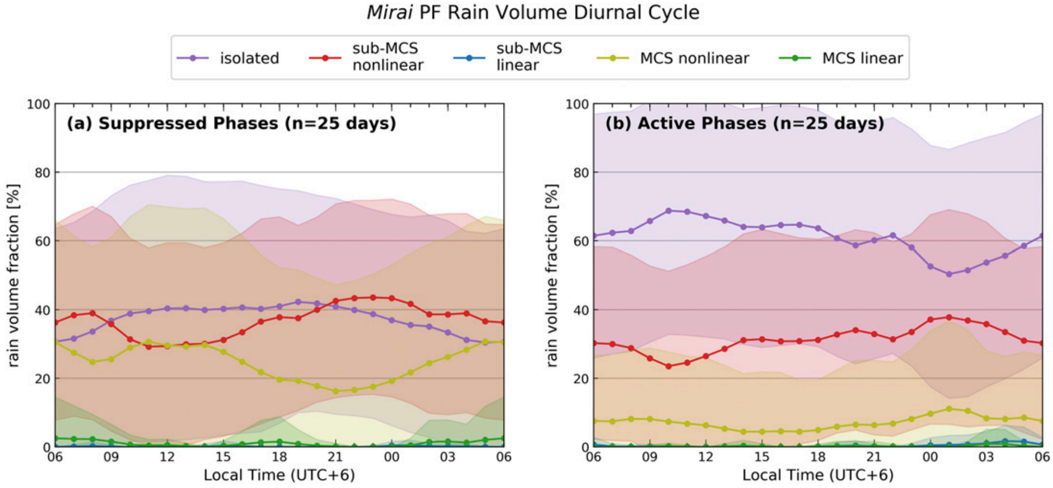

FIG. 16. As in Fig. 12, but for the *Mirai*.

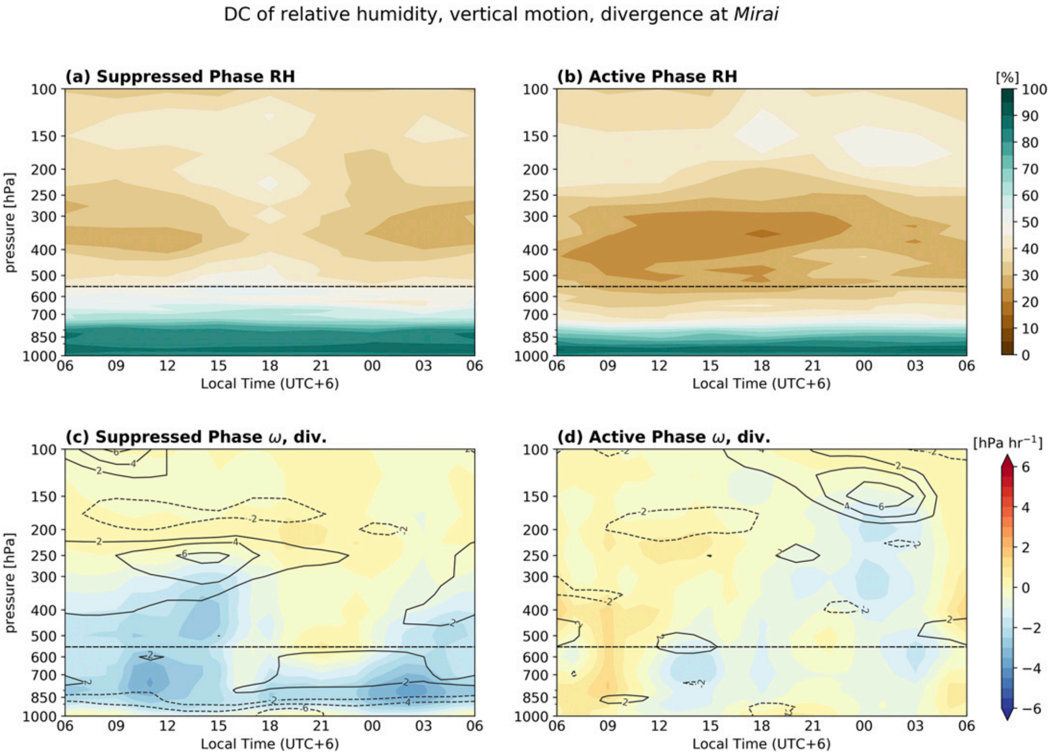

FIG. 17. As in Fig. 13, but for the *Mirai*.

than at the *Revelle* due to the influence of the southeasterly trades (Fig. 18c; Kerns and Chen 2014). There was little diurnal variability in CAPE, and CAPE was about half of what was observed at the *Revelle* (Fig. 18d).

Latent heat fluxes were higher at the *Mirai* than at the *Revelle*, most likely due to stronger surface winds (Fig. 18e). However, there was no diurnal variability in the latent heat fluxes, which mostly resembled the weak variability in winds. The variability in Δq was lower than at the *Revelle*, with peaks occurring around 1400 LT, consistent with the peak in solar heating. (Fig. 18f). During the suppressed phase, a broad maximum in sensible heat flux was achieved in the afternoon, and a second peak was observed at sunrise (Fig. 18g). This DC in sensible heat flux during the suppressed phase was statistically significant and was consistent with the DC of ΔT (Fig. 18h), with the afternoon peak due to a weak increase in SST, and the morning maximum due to a decrease in near-surface temperature. The active phase showed much weaker

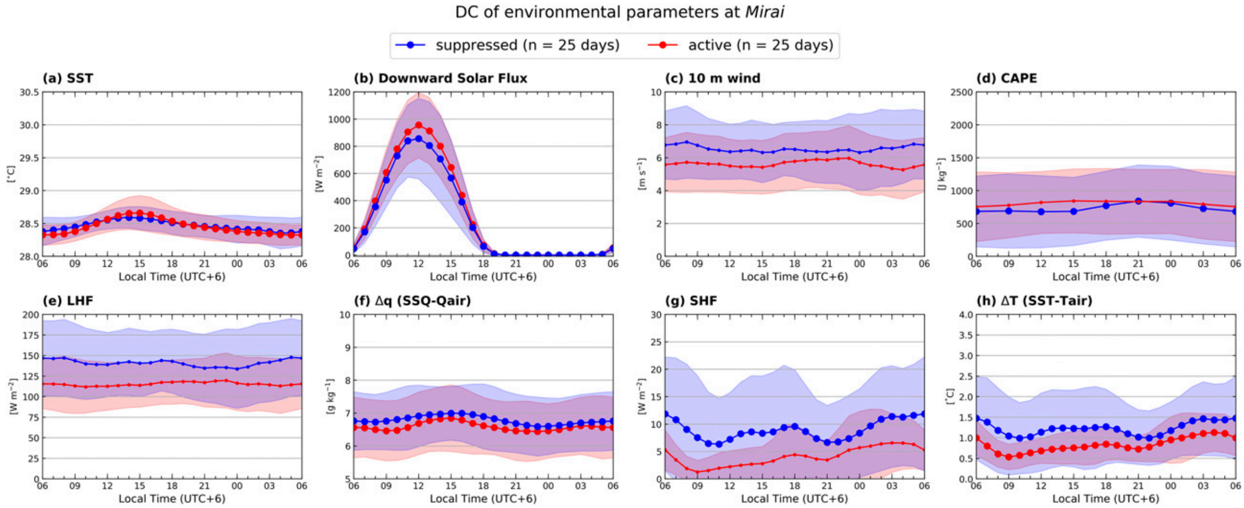

FIG. 18. As in Fig. 14, but for the *Mirai*.

sensible heat flux values, with a single maximum occurring near 0300 LT. This corresponded well with ΔT, as well as the secondary peak in rain rates (Fig. 15b).

6. Discussion and summary

This study focused on comparing PFs (isolated, sub-MCS nonlinear, sub-MCS linear, MCS nonlinear, and MCS linear) between suppressed and active phases of the MJO at two locations within the central IO during DYNAMO. In the MJO evolution section, we showed that the large-scale environments differed on- and off-equator during both MJO events. In the suppressed phase of October, there was weak vertical motion and little surface convergence observed over the *Revelle*, the atmospheric column was dry, and there were no large rain events observed. South of the equator, the ITCZ was present near the *Mirai* and embedded within the ITCZ were some large mesoscale systems (Ciesielski et al. 2018). As the MJO entered the active phase toward the end of October, the maximum in upward motion shifted toward the equator and there was a steady moistening of the column observed over the *Revelle* corresponding to high-intensity but short-lived mesoscale systems. Over the *Mirai*, weak subsidence was prevalent and a strong dry-air intrusion from the subtropics suppressed convection (Kerns and Chen 2014).

After the first MJO exited the region, there was little large-scale vertical motion within this area of the deep tropics and drier conditions were found over the *Revelle* and *Mirai*, limiting mesoscale activity. Toward the end of November though, widespread upward motion dominated. Large, persistent systems were observed over the *Revelle* that had a considerable stratiform rainfall component. These events coincided with two WWBs with enhanced surface convergence that propagated eastward across the central IO. Also during this time, a strong stable layer developed near the 0°C level associated with the stratiform region. Over the *Mirai*, an increase in mesoscale activity happened within the last 2 days of the observing period, which contributed significantly to the total rainfall observed.

The percentage of PFs observed during the active and suppressed phases near the *Revelle* and *Mirai* was fairly similar, with isolated features representing about 90%–95% of the total population. However, upon closer analysis, we found that these features contributed nearly 40% to the total rain volume during the suppressed phase at the *Revelle*, and only around 10% during the active phase and during both phases at the *Mirai*. At the *Revelle*, sub-MCS nonlinear, sub-MCS linear, MCS nonlinear, and MCS linear features all occurred more frequently during the active phase compared to the suppressed phase. MCS nonlinear features contributed the most to the rain volume during the active phase, and environmental parameters such as total precipitable water, air–sea fluxes, SST, and surface moisture were all larger on average, which was statistically significant.

A similar but reversed pattern was observed at the *Mirai*, although the differences between suppressed and active phases off-equator were not nearly as extreme compared to the *Revelle*. At the *Mirai*, sub-MCS nonlinear and MCS nonlinear features were more prevalent during the suppressed phase, with MCS nonlinear features contributing the most to the total rain volume during this phase. Once again, total precipitable water, air–sea fluxes, SST, and surface-level moisture, in addition to surface winds, were all larger during the suppressed phase. Additionally, during both phases on- and off-equator 30-dBZ echo-top heights increased with increasing size and degree of organization. Isolated features had the lowest 30-dBZ heights near the 0°C level, while MCS linear features had the tallest 30-dBZ echoes around 9 km.

The DC of rainfall varied significantly on average between the suppressed and active phases at the *Revelle*. During the suppressed phase, two local peaks in rainfall were observed in the afternoon and just after midnight. These weak enhancements corresponded to an increase in the sub-MCS nonlinear and MCS nonlinear rain volume fractions. The afternoon peak was likely driven by solar heating, which increased SST and air–sea fluxes, and a maximum in surface convergence was observed. The later peak in rainfall coincided with the maximum in CAPE and may have been driven by radiative cooling of the mid- to upper troposphere, although more analysis is needed to state this with certainty. The DC during the active phase was much stronger, and a single peak in rainfall occurred just after midnight, consistent with other studies regarding the DC of tropical oceanic convection in the active MJO phases (Sui et al. 1997; Tian et al. 2006; Suzuki 2009; Sakaeda et al. 2017, 2018; Rowe et al. 2019). Rain rates were 5–10 mm day^{-1} greater during the active phase, and the maximum near midnight corresponded to an increase in MCS nonlinear rain volume fraction (which started in the afternoon). This increase in MCS nonlinear rain volume fraction also coincided with column moistening and enhanced vertical motion throughout the afternoon. Solar heating was reduced due to increased cloudiness and likely played a role in reducing the DC of SST. Isolated and sub-MCS nonlinear features contributed the most to the rain volume during the afternoon, but this had little effect on the DC compared to the larger MCS events that reached peak maturity in the early morning hours.

Using data from the NCAR S-pol radar on Gan Island, Rowe et al. (2019) showed that the DCs observed during the active phases of MJO1 and MJO2 differed. We also analyzed this at the *Revelle* and found the amplitude of the DC of MCS nonlinear rain volume fraction was reduced from 40% in MJO1 to 20% in MJO2. There was much less variability in the DC of overall precipitation during MJO2 as well. These differences can be inferred from the time series where rain events in MJO1 were more episodic in nature, while rain events in MJO2 were longer lived and produced significantly more stratiform rain. Enhanced convection in MJO2 coincided with the passage of a strong Kelvin wave (Gottschalck et al. 2013) which forced two WWBs. These WWBs significantly enhanced the feedback between the ocean and atmosphere through air–sea fluxes and deep wind shear and were associated with strong surface-level convergence, which allowed for convection to persist, thus reducing the DC. Hence, these results agree with Rowe et al. (2019) and demonstrate that features such as synoptic waves can influence the DC of rainfall.

The DC of rainfall observed over the *Mirai* was fairly different from the *Revelle*. Rain rates were higher during the suppressed phase at the *Mirai*, but only reached a maximum of ~6 mm day^{-1} (compared to 14 mm day^{-1} during the active phase at the *Revelle*). The DC during the suppressed phase was quite weak, while the DC during the active phase had a bimodal distribution with peaks in the afternoon and early morning (consistent with the suppressed phase on-equator). The diurnal variability of MCS nonlinear rain volume fraction was greatest during the suppressed phase, in which peak rain volume contribution was achieved at sunrise. Furthermore, the diurnal variability of MCS nonlinear rain volume fraction during the active phase off-equator was basically the same as that during the suppressed phase on-equator. The mean DCs of environmental parameters off-equator were similar between suppressed and active phases, suggesting some additional factors may be playing a larger role in the DC of precipitation.

This study highlighted the impacts of the local environment on the DC of precipitation and convective organization within the MJO and local differences in the DC within the central IO. Unfortunately, the analysis was limited to the two coherent MJOs observed during the DYNAMO intensive observing period. Thus, future work may involve a similar analysis from a climatological perspective, identifying PFs from TRMM/GPM radar. With additional data, the evolution of PFs and the DC of PFs between specific phases of the MJO (e.g., phases 1–8 rather than suppressed versus active) could also be investigated. Additionally, this study was limited to only analyzing observations. Modeling experiments could be designed to determine the major factors that contribute to the evolution of PFs and precipitation on the intraseasonal and diurnal time scales within the central IO.

Acknowledgments. This research was supported by NSF DYNAMO Project Grant AGS-1649784. We thank the radar meteorology group at CSU, especially Paul Hein, Brenda Dolan, Weixin Xu, and Kyle Chudler, for assistance in acquiring and processing data, and for insightful science discussions. We also thank Chris Fairall, Elizabeth Thompson, Masaki Katsumata, and Osamu Tsukamoto for their discussions on air–sea fluxes and the COARE bulk flux algorithm, and Hungjui Yu for providing helpful suggestions regarding the methodology. Additionally, we thank the three anonymous reviewers for their constructive comments. The DYNAMO legacy dataset can be found at https://data.eol.ucar.edu/project/574.

REFERENCES

Barnes, H. C., and R. A. Houze Jr., 2013: The precipitating cloud population of the Madden-Julian oscillation over the Indian and west Pacific Oceans. *J. Geophys. Res.*, **118**, 6996–7023, https://doi.org/10.1002/jgrd.50375.

Bechtold, P., M. Köhler, T. Jung, F. Doblas-Reyes, M. Leutbecher, M. J. Rodwell, F. Vitart, and G. Balsamo, 2008: Advances in simulating atmospheric variability with the ECMWF model: From synoptic to decadal time-scales. *Quart. J. Roy. Meteor. Soc.*, **134**, 1337–1351, https://doi.org/10.1002/qj.289.

Bellenger, H., Y. N. Takayabu, T. Ushiyama, and K. Yoneyama, 2010: Role of diurnal warm layers in the diurnal cycle of convection over the tropical Indian Ocean during MISMO. *Mon. Wea. Rev.*, **138**, 2426–2433, https://doi.org/10.1175/2010MWR3249.1.

Benedict, J. J., and D. A. Randall, 2009: Structure of the Madden–Julian oscillation in the superparameterized CAM. *J. Atmos. Sci.*, **66**, 3277–3296, https://doi.org/10.1175/2009JAS3030.1.

Chen, S. S., and R. A. Houze Jr., 1997: Diurnal variation and lifecycle of deep convective systems over the tropical Pacific warm pool. *Quart. J. Roy. Meteor. Soc.*, **123**, 357–388, https://doi.org/10.1002/qj.49712353806.

Cheng, W.-Y., D. Kim, and A. Rowe, 2018: Objective quantification of convective clustering observed during the AMIE/DYNAMO two-day rain episodes. *J. Geophys. Res. Atmos.*, **123**, 10 361–10 378, https://doi.org/10.1029/2018JD028497.

Ciesielski, P. E., and Coauthors, 2014: Quality-controlled upper-air sounding dataset for DYNAMO/CINDY/AMIE: Development and corrections. *J. Atmos. Oceanic Technol.*, **31**, 741–764, https://doi.org/10.1175/JTECH-D-13-00165.1.

——, R. H. Johnson, W. H. Schubert, and J. H. Ruppert Jr., 2018: Diurnal cycle of the ITCZ in DYNAMO. *J. Climate*, **31**, 4543–4562, https://doi.org/10.1175/JCLI-D-17-0670.1.

Copernicus Climate Change Service, 2017: ERA5: Fifth generation of ECMWF atmospheric reanalyses of the global climate. Copernicus Climate Change Service Climate Data Store, accessed 23 October 2020, https://cds.climate.copernicus.eu/cdsapp#!/home.

DeMott, C. A., and S. A. Rutledge, 1998: The vertical structure of TOGA COARE convection. Part II: Modulating influences and implications for diabatic heating. *J. Atmos. Sci.*, **55**, 2748–2762, https://doi.org/10.1175/1520-0469(1998)055<2748:TVSOTC>2.0.CO;2.

de Szoeke, S. P., J. B. Edson, J. R. Marion, C. W. Fairall, and L. Bariteau, 2015: The MJO and air–sea interaction in TOGA COARE and DYNAMO. *J. Climate*, **28**, 597–622, https://doi.org/10.1175/JCLI-D-14-00477.1.

Dolan, B., P. Hein, S. Rutledge, and S. Powell, 2017: DYNAMO legacy rainfall products. UCAR, http://dynamo.ml-ext.ucar.edu/dynamo_legacy/.

Edson, J. B., and Coauthors, 2013: On the exchange of momentum over the open ocean. *J. Phys. Oceanogr.*, **43**, 1589–1610, https://doi.org/10.1175/JPO-D-12-0173.1.

——, C. Fairall, S. de Szoeke, J. N. Moum, and B. W. Kerns, 2017: R/V Roger Revelle flux, near-surface meteorology, and navigation data. UCAR, accessed 20 May 2019, https://doi.org/10.5065/D6KP80J9.

Fairall, C. W., E. F. Bradley, D. P. Rogers, J. B. Edson, and G. S. Young, 1996: Bulk parameterization of air–sea fluxes for TOGA COARE. *J. Geophys. Res.*, **101**, 3747–3764, https://doi.org/10.1029/95JC03205.

——, ——, J. E. Hare, A. A. Grachev, and J. B. Edson, 2003: Bulk parameterization of air–sea fluxes: Updates and verification for the COARE algorithm. *J. Climate*, **16**, 571–591, https://doi.org/10.1175/1520-0442(2003)016<0571:BPOASF>2.0.CO;2.

Gottschalck, J., P. E. Roundy, C. J. Schreck III, A. Vintzileos, and C. Zhang, 2013: Large-scale atmospheric and oceanic conditions during the 2011–12 DYNAMO field campaign. *Mon. Wea. Rev.*, **141**, 4173–4196, https://doi.org/10.1175/MWR-D-13-00022.1.

Grant, L. D., T. P. Lane, and S. C. van den Heever, 2018: The role of cold pools in tropical oceanic convective systems. *J. Atmos. Sci.*, **75**, 2615–2634, https://doi.org/10.1175/JAS-D-17-0352.1.

Gray, W. M., and R. W. Jacobson, 1977: Diurnal variation of deep cumulus convection. *Mon. Wea. Rev.*, **105**, 1171–1188, https://doi.org/10.1175/1520-0493(1977)105<1171:DVODCC>2.0.CO;2.

Harrison, D. E., and G. A. Vecchi, 1997: Westerly wind events in the tropical Pacific, 1986–95. *J. Climate*, **10**, 3131–3156, https://doi.org/10.1175/1520-0442(1997)010<3131:WWEITT>2.0.CO;2.

Houze, R. A., Jr., 2004: Mesoscale convective systems. *Rev. Geophys.*, **42**, RG4003, https://doi.org/10.1029/2004RG000150.

Huffman, G. J., and Coauthors, 2007: The TRMM Multisatellite Precipitation Analysis (TMPA): Quasi-global, multiyear, combined-sensor precipitation estimates at fine scales. *J. Hydrometeor.*, **8**, 38–55, https://doi.org/10.1175/JHM560.1.

Hung, M.-P., J.-L. Lin, W. Wang, D. Kim, T. Shinoda, and S. J. Weaver, 2013: MJO and convectively coupled equatorial waves simulated by CMIP5 climate models. *J. Climate*, **26**, 6185–6214, https://doi.org/10.1175/JCLI-D-12-00541.1.

Jabouille, P., J. L. Redelsperger, and J. P. Lafore, 1996: Modification of surface fluxes by atmospheric convection in the TOGA COARE region. *Mon. Wea. Rev.*, **124**, 816–837, https://doi.org/10.1175/1520-0493(1996)124<0816:MOSFBA>2.0.CO;2.

Janowiak, J. E., P. A. Arkin, and M. Morrissey, 1994: An examination of the diurnal cycle in oceanic tropical rainfall using satellite and in situ data. *Mon. Wea. Rev.*, **122**, 2296–2311, https://doi.org/10.1175/1520-0493(1994)122<2296:AEOTDC>2.0.CO;2.

Johnson, R. H., and M. E. Nicholls, 1983: Composite analysis of the boundary layer accompanying a tropical squall line. *Mon. Wea. Rev.*, **111**, 308–319, https://doi.org/10.1175/1520-0493(1983)111<0308:ACAOTB>2.0.CO;2.

——, and P. E. Ciesielski, 2013: Structure and properties of Madden–Julian oscillations deduced from DYNAMO sounding arrays. *J. Atmos. Sci.*, **70**, 3157–3179, https://doi.org/10.1175/JAS-D-13-065.1.

——, ——, and K. A. Hart, 1996: Tropical inversions near the 0°C level. *J. Atmos. Sci.*, **53**, 1838–1855, https://doi.org/10.1175/1520-0469(1996)053<1838:TINTL>2.0.CO;2.

——, T. M. Rickenbach, S. A. Rutledge, P. E. Ciesielski, and W. H. Schubert, 1999: Trimodal characteristics of tropical convection. *J. Climate*, **12**, 2397–2418, https://doi.org/10.1175/1520-0442(1999)012<2397:TCOTC>2.0.CO;2.

Katsumata, M., T. Ushiyama, K. Yoneyama, and Y. Fujiyoshi, 2008: Combined use of TRMM/PR and disdrometer data to correct reflectivity of ground-based radars. *SOLA*, **4**, 101–104, https://doi.org/10.2151/sola.2008-026.

Kerns, B. W., and S. S. Chen, 2014: Equatorial dry air intrusion and related synoptic variability in MJO initiation during DYNAMO. *Mon. Wea. Rev.*, **142**, 1326–1343, https://doi.org/10.1175/MWR-D-13-00159.1.

Kim, D., and Coauthors, 2009: Application of MJO simulation diagnostics to climate models. *J. Climate*, **22**, 6413–6436, https://doi.org/10.1175/2009JCLI3063.1.

Kummerow, C., W. Barnes, T. Kozu, J. Shiue, and J. Simpson, 1998: The Tropical Rainfall Measuring Mission (TRMM) sensor package. *J. Atmos. Oceanic Technol.*, **15**, 809–817, https://doi.org/10.1175/1520-0426(1998)015<0809:TTRMMT>2.0.CO;2.

Lau, W. K.-M., and H.-T. Wu, 2010: Characteristics of precipitation, cloud, and latent heating associated with the Madden–Julian oscillation. *J. Climate*, **23**, 504–518, https://doi.org/10.1175/2009JCLI2920.1.

Lin, J., B. Mapes, M. Zhang, and M. Newman, 2004: Stratiform precipitation, vertical heating profiles, and the Madden–Julian oscillation. *J. Atmos. Sci.*, **61**, 296–309, https://doi.org/10.1175/1520-0469(2004)061<0296:SPVHPA>2.0.CO;2.

——, and Coauthors, 2006: Tropical intraseasonal variability in 14 IPCC AR4 climate models. Part I: Convective signals. *J. Climate*, **19**, 2665–2690, https://doi.org/10.1175/JCLI3735.1.

Liu, C., and E. Zipser, 2013: Regional variation of morphology of organized convection in the tropics and subtropics. *J. Geophys. Res. Atmos.*, **118**, 453–466, https://doi.org/10.1029/2012JD018409.

——, ——, D. J. Cecil, S. W. Nesbitt, and S. Sherwood, 2008: A cloud and precipitation feature database from nine years of TRMM observations. *J. Appl. Meteor. Climatol.*, **47**, 2712–2728, https://doi.org/10.1175/2008JAMC1890.1.

Madden, R. A., and P. R. Julian, 1971: Detection of a 40–50 day oscillation in the zonal wind in the tropical Pacific. *J. Atmos. Sci.*, **28**, 702–708, https://doi.org/10.1175/1520-0469(1971)028<0702:DOADOI>2.0.CO;2.

——, and ——, 1972: Description of global-scale circulation cells in the tropics with a 40–50 day period. *J. Atmos. Sci.*, **29**, 1109–1123, https://doi.org/10.1175/1520-0469(1972)029<1109:DOGSCC>2.0.CO;2.

Medioni, G., M.-S. Lee, and C. K. Tang, 2000: *A Computational Framework for Segmentation and Grouping*. Elsevier, 260 pp.

Moum, J. N., and Coauthors, 2014: Air–sea interactions from the westerly wind burst events during the November 2011 MJO in the Indian Ocean. *Bull. Amer. Meteor. Soc.*, **95**, 1185–1199, https://doi.org/10.1175/BAMS-D-12-00225.1.

Nesbitt, S. W., E. J. Zipser, and D. J. Cecil, 2000: A census of precipitation features in the tropics using TRMM: Radar, ice scattering, and lightning observations. *J. Climate*, **13**, 4087–4106, https://doi.org/10.1175/1520-0442(2000)013<4087:ACOPFI>2.0.CO;2.

——, R. Cifelli, and S. A. Rutledge, 2006: Storm morphology and rainfall characteristics of TRMM precipitation features. *Mon. Wea. Rev.*, **134**, 2702–2721, https://doi.org/10.1175/MWR3200.1.

Petersen, W. A., S. A. Rutledge, and R. E. Orville, 1996: Cloud–to–ground lightning observations from TOGA COARE: Selected results and lightning location algorithms. *Mon. Wea. Rev.*, **124**, 602–620, https://doi.org/10.1175/1520-0493(1996)124<0602:CTGLOF>2.0.CO;2.

Powell, S. W., 2016: Updraft buoyancy within and moistening by cumulonimbi prior to MJO convective onset in a regional model. *J. Atmos. Sci.*, **73**, 2913–2934, https://doi.org/10.1175/JAS-D-15-0326.1.

——, and R. A. Houze Jr., 2015: Evolution of precipitation and convective echo top heights observed by TRMM radar over the Indian Ocean during DYNAMO. *J. Geophys. Res. Atmos.*, **120**, 3906–3919, https://doi.org/10.1002/2014JD022934.

——, ——, and S. R. Brodzik, 2016: Rainfall-type categorization of radar echoes using polar coordinate reflectivity data. *J. Atmos. Oceanic Technol.*, **33**, 523–538, https://doi.org/10.1175/JTECH-D-15-0135.1.

Randall, D. A., M. Khairoutdinov, A. Arakawa, and W. Grabowski, 2003: Breaking the cloud parameterization deadlock. *Bull. Amer. Meteor. Soc.*, **84**, 1547–1564, https://doi.org/10.1175/BAMS-84-11-1547.

Rickenbach, T. M., and S. A. Rutledge, 1998: Convection in TOGA COARE: Horizontal scale, morphology, and rainfall production. *J. Atmos. Sci.*, **55**, 2715–2729, https://doi.org/10.1175/1520-0469(1998)055<2715:CITCHS>2.0.CO;2.

Riley, E. M., B. E. Mapes, and S. N. Tulich, 2011: Clouds associated with the Madden–Julian oscillation: A new perspective from *CloudSat*. *J. Atmos. Sci.*, **68**, 3032–3051, https://doi.org/10.1175/JAS-D-11-030.1.

Rotunno, R., J. B. Klemp, and M. L. Weisman, 1988: A theory for strong, long-lived squall lines. *J. Atmos. Sci.*, **45**, 463–485, https://doi.org/10.1175/1520-0469(1988)045<0463:ATFSLL>2.0.CO;2.

Rowe, A. K., R. A. Houze Jr., S. Brodzik, and M. D. Zuluaga, 2019: The diurnal and microphysical characteristics of MJO rain events during DYNAMO. *J. Atmos. Sci.*, **76**, 1975–1988, https://doi.org/10.1175/JAS-D-18-0316.1.

Ruppert, J. H., Jr., and R. H. Johnson, 2015: Diurnally modulated cumulus moistening in the preonset stage of the

Madden–Julian oscillation during DYNAMO. *J. Atmos. Sci.*, **72**, 1622–1647, https://doi.org/10.1175/JAS-D-14-0218.1.

Sakaeda, N., G. N. Kiladis, and J. Dias, 2017: The diurnal cycle of tropical cloudiness and rainfall associated with the Madden–Julian oscillation. *J. Atmos. Sci.*, **30**, 3999–4020, https://doi.org/10.1175/JCLI-D-16-0788.1.

——, S. W. Powell, J. Dias, and G. N. Kiladis, 2018: The diurnal variability of precipitating cloud populations during DYNAMO. *J. Atmos. Sci.*, **75**, 1307–1326, https://doi.org/10.1175/JAS-D-17-0312.1.

Saxen, T. R., and S. A. Rutledge, 1998: Surface fluxes and boundary layer recovery in TOGA COARE: Sensitivity to convective organization. *J. Atmos. Sci.*, **55**, 2763–2781, https://doi.org/10.1175/1520-0469(1998)055<2763:SFABLR>2.0.CO;2.

Skyllingstad, E. D., S. P. de Szoeke, and L. W. O'Neill, 2019: Modeling the transient response of tropical convection to mesoscale SST variations. *J. Atmos. Sci.*, **76**, 1227–1244, https://doi.org/10.1175/JAS-D-18-0079.1.

Smull, B. F., and R. A. Houze Jr., 1985: A midlatitude squall line with a trailing region of stratiform rain: Radar and satellite observations. *Mon. Wea. Rev.*, **113**, 117–133, https://doi.org/10.1175/1520-0493(1985)113<0117:AMSLWA>2.0.CO;2.

Steiner, M., R. A. Houze Jr., and S. E. Yuter, 1995: Climatological characterization of three-dimensional storm structure from operational radar and rain gauge data. *J. Appl. Meteor.*, **34**, 1978–2007, https://doi.org/10.1175/1520-0450(1995)034<1978:CCOTDS>2.0.CO;2.

Sui, C.-H., K.-M. Lau, Y. N. Takayabu, and D. A. Short, 1997: Diurnal variations in tropical oceanic cumulus convection during TOGA COARE. *J. Atmos. Sci.*, **54**, 639–655, https://doi.org/10.1175/1520-0469(1997)054<0639:DVITOC>2.0.CO;2.

Suzuki, T., 2009: Diurnal cycle of deep convection in super clusters embedded in the Madden–Julian oscillation. *J. Geophys. Res.*, **114**, D22102, https://doi.org/10.1029/2008JD011303.

Takemi, T., 2015: Relationship between cumulus activity and environmental moisture during the CINDY2011/DYNAMO field experiment as revealed from convection-resolving simulations. *J. Meteor. Soc. Japan*, **93A**, 41–58, https://doi.org/10.2151/jmsj.2015-035.

Thompson, E. J., S. A. Rutledge, B. Dolan, and M. Thurai, 2015: Drop size distributions and radar observations of convective and stratiform rain over the equatorial Indian and west Pacific Oceans. *J. Atmos. Sci.*, **72**, 4091–4125, https://doi.org/10.1175/JAS-D-14-0206.1.

——, J. N. Moum, C. W. Fairall, and S. A. Rutledge, 2018: Wind limits on rain layers and diurnal warm layers. *J. Geophys. Res. Oceans*, **124**, 897–924, https://doi.org/10.1029/2018JC014130.

Tian, B., D. E. Waliser, and E. J. Fetzer, 2006: Modulation of the diurnal cycle of tropical deep convective clouds by the MJO. *Geophys. Res. Lett.*, **33**, L20704, https://doi.org/10.1029/2006GL027752.

Vitart, F., and F. Molteni, 2010: Simulation of the Madden–Julian oscillation and its teleconnections in the ECMWF forecast system. *Quart. J. Roy. Meteor. Soc.*, **136**, 842–855, https://doi.org/10.1002/qj.623.

Weisman, M. L., and R. Rotunno, 2004: "A theory of strong long-lived squall lines" revisited. *J. Atmos. Sci.*, **61**, 361–382, https://doi.org/10.1175/1520-0469(2004)061<0361:ATFSLS>2.0.CO;2.

——, J. B. Klemp, and R. Rotunno, 1988: Structure and evolution of numerically simulated squall lines. *J. Atmos. Sci.*, **45**, 1990–2013, https://doi.org/10.1175/1520-0469(1988)045<1990:SAEONS>2.0.CO;2.

Wheeler, M., and H. H. Hendon, 2004: An all-season real-time multivariate MJO index: Development of an index for monitoring and prediction. *Mon. Wea. Rev.*, **132**, 1917–1932, https://doi.org/10.1175/1520-0493(2004)132<1917:AARMMI>2.0.CO;2.

Xu, W., and S. A. Rutledge, 2014: Convective characteristics of the Madden–Julian oscillation over the central Indian Ocean observed by shipborne radar during DYNAMO. *J. Atmos. Sci.*, **71**, 2859–2877, https://doi.org/10.1175/JAS-D-13-0372.1.

——, and ——, 2015: Morphology, intensity, and rainfall production of MJO convection: Observations from DYNAMO shipborne radar and TRMM. *J. Atmos. Sci.*, **72**, 623–640, https://doi.org/10.1175/JAS-D-14-0130.1.

——, and ——, 2016: Time scales of shallow-to-deep convective transition associated with the onset of Madden-Julian oscillations. *Geophys. Res. Lett.*, **43**, 2880–2888, https://doi.org/10.1002/2016GL068269.

——, ——, C. Schumacher, and M. Katsumata, 2015: Evolution, properties, and spatial variability of MJO convection near and off the equator during DYNAMO. *J. Atmos. Sci.*, **72**, 4126–4147, https://doi.org/10.1175/JAS-D-15-0032.1.

Yamada, H., K. Yoneyama, M. Katsumata, and R. Shirooka, 2010: Observations of a super cloud cluster accompanied by synoptic-scale eastward-propagating precipitating systems over the Indian Ocean. *J. Atmos. Sci.*, **67**, 1456–1473, https://doi.org/10.1175/2009JAS3151.1.

Yang, G.-Y., and J. Slingo, 2001: The diurnal cycle in the tropics. *Mon. Wea. Rev.*, **129**, 784–801, https://doi.org/10.1175/1520-0493(2001)129<0784:TDCITT>2.0.CO;2.

Yokoi, S. M. K., and K. Yoneyama, 2014: Variability in surface meteorology and air–sea fluxes due to cumulus convective systems observed during CINDY/DYNAMO. *J. Geophys. Res.*, **119**, 2064–2078, https://doi.org/10.1002/2013JD020621.

Yoneyama, K., C. Zhang, and C. N. Long, 2013: Tracking pulses of the Madden–Julian oscillation. *Bull. Amer. Meteor. Soc.*, **94**, 1871–1891, https://doi.org/10.1175/BAMS-D-12-00157.1.

Yu, H., R. H. Johnson, P. E. Ciesielski, and H.-C. Kuo, 2018: Observation of quasi-2-day convective disturbances in the equatorial Indian Ocean during DYNAMO. *J. Atmos. Sci.*, **75**, 2867–2888, https://doi.org/10.1175/JAS-D-17-0351.1.

Zelinsky, R. C., C. Zhang, and C. Liu, 2019: The relationship between the ITCZ and MJO initiation over the Indian Ocean. *J. Atmos. Sci.*, **76**, 2275–2294, https://doi.org/10.1175/JAS-D-18-0327.1.

Zhang, C., 2005: Madden–Julian oscillation. *Rev. Geophys.*, **43**, RG2003, https://doi.org/10.1029/2004RG000158.

——, 2013: Madden–Julian oscillation: Bridging weather and climate. *Bull. Amer. Meteor. Soc.*, **94**, 1849–1870, https://doi.org/10.1175/BAMS-D-12-00026.1.

——, M. Dong, S. Gualdi, H. H. Hendon, E. D. Maloney, A. Marshall, K. R. Sperber, and W. Wang, 2006: Simulations of the Madden–Julian oscillation in four pairs of coupled and uncoupled global models. *Climate Dyn.*, **27**, 573–592, https://doi.org/10.1007/s00382-006-0148-2.

Zhao, N., and T. Nasuno, 2020: How does the air-sea coupling frequency affect convection during the MJO passage? *J. Adv. Model. Earth Syst.*, **12**, e2020MS002058, https://doi.org/10.1029/2020MS002058.

Zuluaga, M. D., and R. A. Houze Jr., 2013: Evolution of the population of precipitating convective systems over the equatorial Indian Ocean in active phases of the Madden–Julian oscillation. *J. Atmos. Sci.*, **70**, 2713–2725, https://doi.org/10.1175/JAS-D-12-0311.1.